Wake Unsteadiness and Tip Vortex System of Full-Scale Helicopters in Ground Effect

C. Christian Wolf* *Research Scientist*
Armin Weiss *Research Scientist*
Clemens Schwarz *Research Scientist*
Johannes N. Braukmann *Research Scientist*
Stefan Koch *Research Scientist*
Markus Raffel *Professor*
German Aerospace Center (DLR), Göttingen, Germany

The main rotor wakes of the free-flying DLR test helicopters Airbus Bo105 and EC135 were investigated in ground effect during hover, vertical takeoff, and forward flight. A high-speed schlieren system tracked the blade tip vortices at about 60 images per revolution. In addition, a constant temperature anemometry system utilized arrays of fiber film sensors, providing velocity statistics and spectra in the rotor flow. The overall wake structure agreed to preceding studies, but the velocity profiles and tip vortex trajectories were sensitive towards the environmental wind conditions. The tip vortices were observed in the schlieren images up to an age corresponding to about two revolutions below the rotor plane, before developing instabilities and falling below the detection limit. Systematic vortex pairing was found for the Bo105 but not for the EC135. The remnants of the tip vortices were identified further downstream in the wake by means of rotor-harmonic velocity signals, but they play a minor role in comparison to broad-banded turbulent fluctuations with a Kolmogorov-like spectrum. For vertical takeoff cases, the rotor wake had a hover-like structure until breaking down into low-frequency oscillations when exceeding a hub height of approximately 1.4 rotor radii. In forward flight, different types of wake velocity footprints were categorized on the basis of the normalized advance ratio. Blade–vortex interactions were found in the frontal area of the main rotor planes and between the main rotor tip vortices and the Bo105's tail rotor. The interactions prevent a further evolution of the tip vortices.

Nomenclature

A, B, C	calibration parameters in King's law
C_T	rotor thrust coefficient
E_{CTA}	CTA sensor output voltage, V
f	frequency, Hz
g	gravitational acceleration, $g = 9.81$ m/s^2
h	normalized rotor hub height, $h = y/R$
m	helicopter gross mass, kg
N_b	number of blades
n	load factor
R	rotor radius, m
T_{CTA}	fiber film sensor temperature, K
T_∞	flow temperature, K
t	time, s or ms
u, v, w	flow velocity components in x, y, z-directions, m/s
V	CTA-measured velocity, $V = \sqrt{u^2 + v^2}$, m/s
V_h	hover-induced velocity, m/s
V_{tip}	rotor tip speed, m/s
$V_{w,x}$	x-component of the tower wind reading, m/s
V_x,V_y	longitudinal, vertical helicopter velocity, m/s
x, y, z	Cartesian coordinates, m
Δ	difference between two values
ρ	air density, kg/m^3
σ	standard deviation
Ψ	azimuth angle, deg
Ψ_{V}	vortex age, deg
Ω	main rotor frequency, rad/s

Abbreviations

BOS	background oriented schlieren technique
BVI	blade–vortex interaction
COH	coherence function
CTA	constant temperature anemometry
DLR	German Aerospace Center
ICAO	International Civil Aviation Organization
IGE	in ground effect
LED	light-emitting diode
MR	main rotor
OGE	outside ground effect
PIV	particle image velocimetry
PSD	power spectral density
SPR	stereo pattern recognition
TR	tail rotor

Introduction

Rotorcraft are surrounded by a complex flow field, which particularly concerns the three-dimensional and unsteady structure of the main rotor wake in ground effect (IGE). Besides the beneficial aspect of a reduced power requirement, the proximity to a ground surface causes a multitude of detrimental impacts. Notable among these are large vibrational loads, a reduced vision due to brownout, and hazards for nearby ground personnel. The wake itself contains an interleaving system of helical tip vortices, which are the primary unsteady features of the flow, and which convect along the slipstream boundary (Refs. 1–3). Starting in the rotor plane, the overall wake development can be divided into three sections as suggested by a comparison to impinging jets (Refs. 4, 5): Region one is the contracting free jet, region two is the transitional area which deflects the flow from vertical into horizontal direction, and region three is the developing wall-parallel jet. Forward motion induces additional large-scale recirculating vortices ahead of the rotor which add further complexity.

*Corresponding author; email: christian.wolf@dlr.de.
Presented at the Vertical Flight Society's 77th Annual Forum & Technology Display, Virtual, May 10–14, 2021. Manuscript received April 2021; accepted August 2021.

Many details and dependencies are not yet fully understood, despite the availability of advanced experimental and numerical tools. A multitude of preceding wake studies in ground effect were conducted for either model rotors in different scales (see Refs. 6–13) or free-flying full-scale helicopters (see Refs. 14–20). The execution of free-flying helicopter experiments is particularly challenging in terms of the selection and implementation of measurement equipment, weather conditions, limited repeatability of test cases, high costs, etc. On the other hand, flight-test data are highly desirable to study the effects of scaling and other differences between simplified laboratory models and true helicopters in an atmospheric environment. In the following, some of the former results with a significant relevance for the current study will be summarized.

Tanner et al. (Ref. 8) performed an IGE wake study on a large model rotor with four blades and a radius of about 1.7 m in the presence of a fuselage model. The experiments were conducted using the U.S. Army General Rotor Model System, with particle image velocimetry (PIV) and five-hole probes acquiring the averaged outwash maps for variations in rotor thrust, hover height, and azimuth angle. PIV has become a standard method to investigate rotor flow fields, particularly in laboratory environments. It can also be used to study instantaneous or phase-averaged flow fields and the derived tip vortex properties, as recently shown by Milluzzo et al. (Refs. 9–11, 21) or Schwarz et al. (Ref. 22).

Silva and Riser (Ref. 17) investigated the IGE wake development of a hovering CH-47D rotorcraft using an array of eight ultrasonic anemometers installed on a remote-controlled cart, measuring the three-component velocity data at an acquisition frequency up to 10 Hz. The tandem rotor setup results in a pronounced azimuthal variation of the outwash velocity, which was investigated with a view to potential hazard for ground personnel and in dependency of the gross mass. The velocity fluctuations showed low-frequency content well below the rotors' blade passing frequencies, which was also found in the wake of a CH-53E helicopter with a conventional main rotor–tail rotor layout (4). The CH-47D full-scale tests were revisited by Ramasamy and Yamauchi (Ref. 5), who investigated a 1/56-scaled model using PIV. Among other results, it was found that the average velocity profile of the rotor outwash shows a good agreement between model scale and full scale when using appropriate normalization. The authors also showed that the formation of large-scale shear vortices, which exceed the size of the tip vortices and form along the outwash boundary, explains low-frequency content in the further wake development (Ref. 23).

Kutz et al. (Ref. 15) performed a combined experimental and numerical study on the IGE wake development of a Hughes 300C light helicopter, particularly focusing on the trajectories of the blade tip vortices. The experiments visualized the vortex positions through fog illumination up to a vortex age of about one revolution below the rotor plane. This early-wake data showed a good agreement to numerical Reynolds-averaged Navier–Stokes solutions, but the further wake development could not be accessed in the experiments due to increasing vortex instabilities preventing a consistent evaluation of the fog images.

Other measurement techniques implemented for IGE wake studies of free-flying helicopters include combinations of ultrasonic anemometers and smoke visualization (Ref. 16), tuft images (Ref. 18), colored chalk visualization (Ref. 19), or arrays of three-cup anemometers (Ref. 20).

Evaluations of rotorcraft in IGE forward flight conditions were pioneered by the work of Sheridan and Wiesner (Ref. 24) and Curtiss et al. (Ref. 25). They showed that the flow pattern depends on the normalized advance ratio, μ^*, defined as the quotient between forward flight velocity and hover-induced velocity,

$$\mu^* = \frac{V_x}{V_h}, \qquad \text{with} \quad V_h = V_{\text{tip}}\sqrt{\frac{C_T}{2}} \tag{1}$$

For values of about $0.4 < \mu^* \leq 0.9$, a large-scale vortex forms ahead of the helicopter. This structure changes the velocity distribution through the rotor plane and partly recirculates turbulent structures or sediment pickup into the inflow of the rotor. The observations were later confirmed and extended (e.g., see Refs. 22, 26–28).

Saijo et al. (Ref. 29) used hot-wire sensors to study the velocity fluctuations in the flow field of a two-bladed model rotor at different advance ratios. A moving belt eliminated the formation of a boundary layer along the ground surface. The impingement of the rotor wake upon the ground caused high-frequency fluctuations reflecting the rotor harmonics. The rotor outwash ahead of the model was governed by broad-banded fluctuations, whereas oscillations of the ground vortex caused low-frequency content at the topological separation point. Ganesh et al. (Refs. 30, 31) conducted similar small-scale experiments with an additional fuselage structure and confirmed of low-frequency content in the rotor wake.

The current experiments follow the study by Schwarz et al. (Ref. 1), who performed an IGE wake evaluation of a free-flying Bo105 helicopter using a background-oriented schlieren system (BOS) for tip vortex tracking and stereoscopic PIV for flow field measurements. The survey was conducted in 2017 and analyzed the wake structure during unsteady maneuvers in comparison to hover conditions or steady forward flight states. The current work was motivated by unanswered questions, incorporating some "lessons learned" regarding the experimental setup, and focusing on the following new aspects:

1) the influence of vortex instabilities and tip vortex pairing on the wake's velocity fluctuations,

2) the repeatability of full-scale tests, and their dependency on both rotorcraft type and environmental conditions, and

3) the role of vortex interactions close to the blade tip during forward flight.

The first aspect tackles that former full-scale studies tracked the blade tip vortices over comparably small ages, for example, corresponding to about one revolution (Refs. 14, 15, 32) or two revolutions (Ref. 1) below the rotor plane. This is partly due to the limited sensitivity and viewing fields of optical measurements, but also due to an early onset of vortex instabilities compared to small-scale measurements. For comparison, Milluzzo et al. (Ref. 21) tracked the tip vortices of one-bladed model rotors with a radius of 0.4 m over at least 4.5 revolutions. To the authors' knowledge, no conclusive explanation for this difference is known, even though connections to the Reynolds-dependent aging of helical vortices (Ref. 33) or the influence of atmospheric turbulence described for fixed-wing tip vortices (Ref. 34) can be made. The current study replaces the PIV system of Ref. 1 with arrays of constant temperature anemometry (CTA) sensors. The CTA technique provides measurements of the wake's velocity signal with a temporal resolution in the kilohertz range. This enables to track the remnants of the tip-vortex–related rotor harmonics into later wake stages and compare their influence on the overall broad-banded velocity spectra.

The second aspect considers that the measurement environment of free-flight tests is less controllable in comparison to wind tunnel or laboratory campaigns. The previous study in Ref. 1 performed an in-depth analysis of a small number of test points, whereas the current study spreads repetitive tests over several days with varying wind conditions. The current work also accounts for two different helicopters, the Airbus Bo105 and EC135, showing distinct differences in the tip-vortex evolution despite being similar types of rotorcraft.

The third aspect uses an enhanced schlieren system with an enlarged field of view, capturing blade–vortex interactions (BVI) occurring close to the rotor plane in forward flight conditions. This explains the absence of an ordered tip-vortex system further downstream in the rotor wake, which was noted in Ref. 1 but could not be explained.

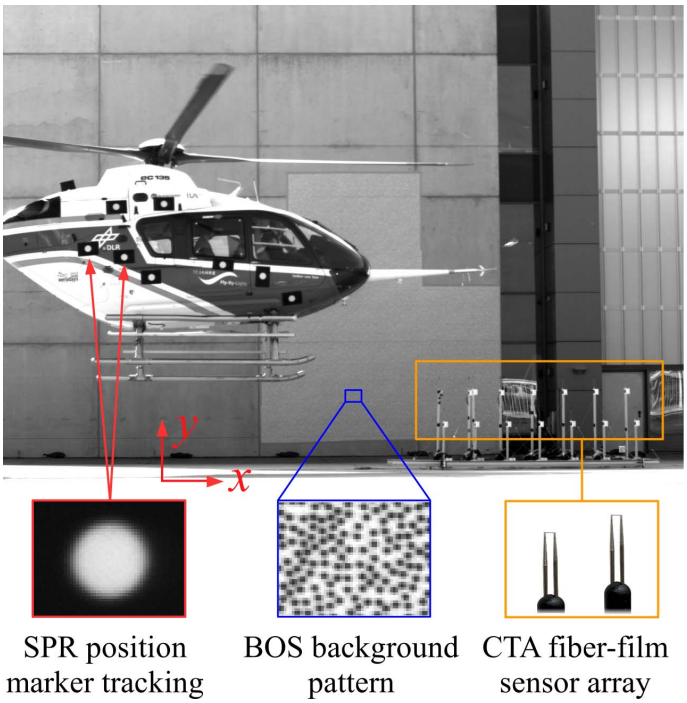

Fig. 1. Hovering EC135 and measurement techniques.

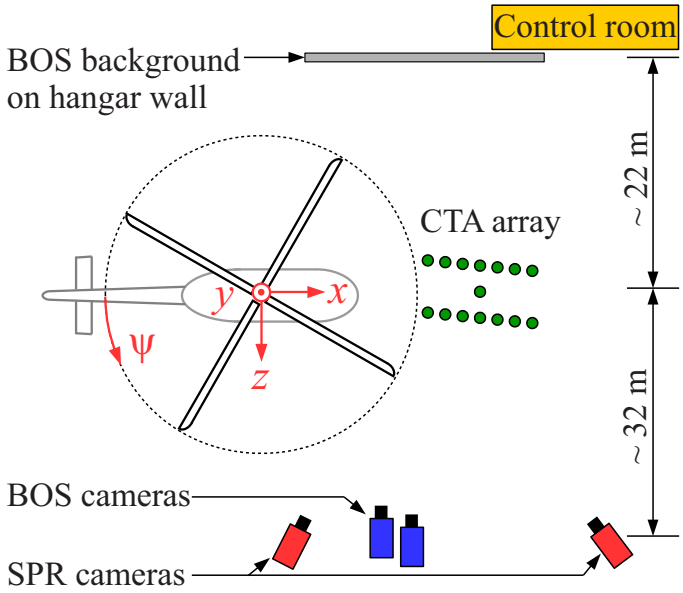

Fig. 2. Sketch of the test setup (not to scale).

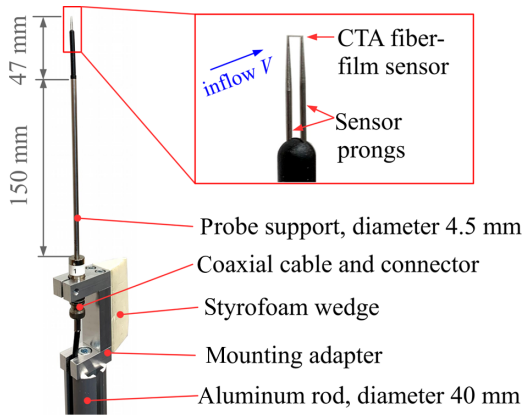

Fig. 3. CTA sensor assembly.

Test setup

The flight tests were conducted in October 2019 at the apron of the DLR facilities within the premises of the Braunschweig regional airport (ICAO–code: EDVE). Several test conditions in ground effect were considered, including hover, vertical takeoff, and low flyover at different speeds. Figure 1 shows DLR's EC135 test helicopter hovering in the test region, and the details below illustrate the three measurement techniques applied in this study: Fuselage markers for stereoscopic position tracking (SPR), a background pattern used for schlieren images (BOS) of the rotor wake, and the constant temperature fiber film array (CTA) used for velocity measurements. All three systems are synchronized using a common data logging system.

Figure 2 is a top–down sketch of the test environment. The origin of the coordinate system is located on the ground, the x-axis is horizontal and points forward along the helicopter's flight path, whereas the y-axis points upwards in vertical direction. The camera systems for SPR and BOS are about 32 m to the right of the helicopter, and the BOS background pattern was attached to a hangar wall about 22 m to the left of the helicopter. The hangar also houses the control room and the data acquisition equipment, connected to the cameras and sensors via long cables. The SPR and BOS techniques were adapted from former DLR full-scale measurements in Refs. 1 and 36.

Constant temperature anemometry

The CTA system was based on an array of up to 17 "TSI 1201" fiber film probes, each featuring a platinum film sensor wrapped around a quartz cylinder with a diameter of 50.8 μm and a sensing width of 1.27 mm. The measurement principle is the same as hot-wire anemometry, but the fiber films are more robust for particle impacts in contaminated flows at the cost of a lower frequency limit. The sensors measure the time-resolved velocity magnitude in a plane parallel to the cylinder axis. Figure 3 shows the entire assembly of a single sensor.

Each sensor was connected via a 50 m coaxial cable to a servo amplifier setup in the control room. The amplifier was developed by DLR for custom CTA arrays, for example, used by Richter et al. (Ref. 37) for transition measurements, and connected to a data recorder with a sampling rate of 50 kHz. The system was adapted to CTA supply cable resistances of about 2.3 Ω including the sensor prongs and plug connectors and to sensor cold resistances of about 5.5 Ω at 273 K. In operation, the servo amplifier regulates the sensor voltage to achieve user-defined sensor hot resistances of about 9.2 Ω. The temperature coefficient of resistance, 0.25%/ K, results in sensor-operating temperatures around $T_{\mathrm{CTA}} = 560$ K. The relation between flow velocity, V, sensor voltage, E_{CTA}, and sensor-to-air temperature difference, $T_{\mathrm{CTA}} - T_\infty$, is governed by the convective heat transfer as predicted by the temperature-linearized King's law (Ref. 38):

$$\frac{E_{\mathrm{CTA}}^2}{T_{\mathrm{CTA}} - T_\infty} = A + B \cdot V^C \tag{2}$$

The parameters A, B, and C were determined for each individual sensor in an a priori wind tunnel calibration run up to $V = 50$ m/s. Equation (2) accounts for variations of the ambient temperature, T_∞, as

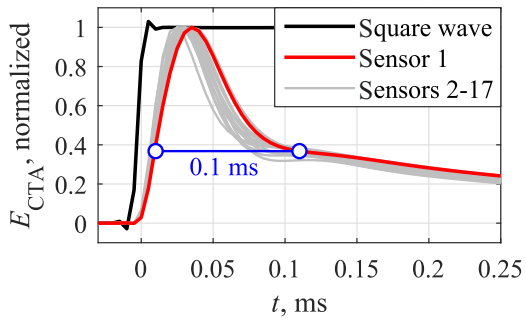

Fig. 4. Square wave test of the CTA sensors.

Fig. 5. Vertical array (top row) and horizontal array (bottom row) of CTA sensors.

measured by dual PT100-temperature probes mounted in the center of the CTA array, and variations of the sensor temperature, T_{CTA}, due to small misadjustments of the servo amplifier. At $V = 10$ m/s, which is approximately the hover-induced velocity V_h of the main rotors, an uncompensated temperature shift of 1 K results in a velocity error of about 0.1 m/s. Therefore, the velocity signal is less reliable when high-frequency thermal eddies of the engine's plume hit the CTA sensors.

The usable velocity frequency band of the sensors was estimated by applying a square wave test signal to the balanced Wheatstone bridge of each sensor. The sensor output signals react with damped natural oscillation peaks as shown in Fig. 4. The individual sensors have slightly different responses, but the width of the peaks and the resulting cutoff frequencies are approximately 0.1 ms and 10 kHz, respectively, when following the argumentation of Freymuth (Ref. 39). Therefore, the current results only consider frequencies up to 10 kHz. This limit is much lower compared to standard hot-wire setups due to the larger thermal capacity of the film sensors and the long supply cables.

The CTA sensors were attached via aluminum rods to a heavy truss structure on the ground. The sensor axes were aligned to measure the instantaneous velocity value in the x, y-plane, $V = \sqrt{u^2 + v^2}$, which is spanned by the rotor-radial and vertical directions (see Figs. 1 and 2). The in-plane velocity error introduced by an out-of-plane velocity component, w, can be neglected due to the large aspect ratio of the fiber films. Two different layouts were applied (see Fig. 5): The "vertical array" measured the outwash velocity profile along the y-direction, whereas the

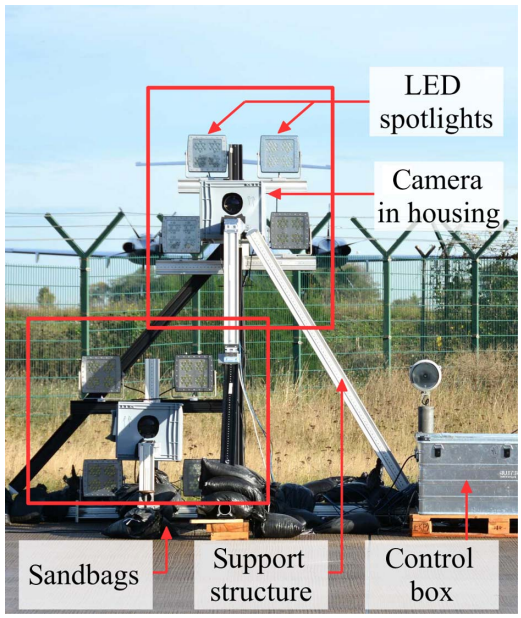

Fig. 6. BOS camera assembly.

two sensor rows of the "horizontal array" covered a larger longitudinal x-range in different heights above ground. The horizontal rows were tilted by 12 deg away from the x-axis to avoid interference with the wake of preceding sensors. The fiber film signals were sampled over at least 60 s for hover test cases, depending on how long the helicopter held a steady position.

Background-oriented schlieren

Schlieren or shadowgraph imaging has been used in rotor flow analysis for decades (Ref. 40), and the newer BOS technique is a versatile, scalable, and easy-to-use schlieren variant. Therefore, BOS is particularly suitable for full-scale or in-flight measurements, for example, demonstrated by Heineck et al. (Ref. 41), Leopold (Ref. 42), Raffel et al. (Ref. 43), or Bauknecht et al. (Refs. 32,44). BOS visualizes schlieren objects by placing a camera and a background pattern with a high optical contrast on opposite sides of the measurement region. Density gradients within the flow, in the current case caused by the blade tip vortices, result in changes of the refractive index and, therefore, apparent shifts of the background pattern.

The BOS setup is similar to the layout used and comprehensively described in Ref. 1, but a new set of two "Phantom VEO 640" high-speed cameras with a larger image sensor size of 2560×1600 pixel and a higher data bandwidth was used. Up to 9000 schlieren images were taken during each hover test point, and an acquisition frequency of 420 Hz enables a time-resolved visualization the tip vortex evolution. Both cameras were equipped with telescopic lenses with a focal length of 300 mm and mounted one above the other on an aluminum truss structure shown in Fig. 6. Four LED flashlights were positioned close to the optical axis of each camera, illuminating a dot pattern adapted to the optical resolution of the cameras and printed on retro-reflective adhesive foil. This setup enables a sufficient signal-to-noise ratio at exposure times down to $\Delta t = 50$ μs. The fields of view are slightly overlapping, with a vertical orientation of the upper camera and a horizontal orientation of the lower camera. The combination of both fields of view forms an "L"-shaped measurement region which follows the curved tip vortex trajectory in ground effect.

Table 1. Test rotorcraft characteristics (see Refs. 45, 46)

Rotorcraft	Bo105	EC135
Main rotor radius, R, m	4.91	5.10
Rotor frequency, Ω, rad/s	$2\pi \cdot 7.07$	$2\pi \cdot 6.58$
Number of blades, N_b	4	4
Airfoil	NACA 23012	DMH 3/4
Chord length, m	0.270	0.288
Blade tip planform	Square	Parabolic
Blade twist, deg/R	-8	-10
Gross mass, m, kg	2070–2230	2760–2910
Hover-induced velocity, V_h, m/s	10.6–11.1	11.8–12.1

The measurement images were cross-correlated with undisturbed reference images using an iterative multipass approach provided by the software "LaVision DaVis 8.4." Random correlation errors in the subpixel range determine the measurement noise, and, hence, the detection limit for density objects in the flow. The results have a grid spacing of about 3.4 mm in both x- and y-directions after applying final interrogation windows of 12 pixel in diameter with an overlap of 75%. The apparent background displacements integrate the density gradients $\partial\rho/\partial x$ and $\partial\rho/\partial y$ along the lines of sight. The blade tip vortices have a minimum density within the core region; hence, the divergence operator is applied to the two-dimensional displacement field. The result represents

$$\frac{\partial^2\rho}{\partial x^2} + \frac{\partial^2\rho}{\partial y^2} \tag{3}$$

with local minima of this scalar quantity marking the projection of the vortex core filaments. The divergence operator also eliminates global background shifts between measurement and reference images, which may occur due to camera vibrations or slight flexure in the camera mounts. The cameras were calibrated in the global x, y-plane using images of a rectangular dot pattern with a spacing of 0.1 m, printed on an aluminum sandwich plate sized 1.5 m × 1.5 m. The out-of-plane z-coordinate of the tip vortices is neglected, resulting in perspective errors.

Position tracking (SPR)

The helicopter flight path was optically tracked at a rate of 12 Hz using two pco.edge 5.5 sCMOS cameras setup in a stereoscopic layout (see Fig. 2) with an included angle of about 45°. The image sensors are sized 2560 × 2160 pixel, and lenses with a focal length of 50 mm were used. The camera calibrations were conducted using several images of a large checkerboard pattern. Seven and eight retro-reflective fiducial markers were attached to the starboard sides of the Bo105 and EC135 helicopters, respectively (see Fig. 1). The markers were illuminated by additional LED spots mounted close to the cameras, allowing for a MATLAB-based automated marker detection and position reconstruction adopted from Schwarz et al. (Ref. 1). The triangulation error of the resulting three-dimensional marker positions was always lower than 10 mm. The in-flight rotor hub position and the fuselage attitude angles were calculated by finding the solid-body transformation between a parked and a free-flying helicopter. The camera fields of view allowed the tracking of the helicopters over about 10 m in both x- and y-direction.

Test rotorcraft

DLR's test rotorcraft are the Bo105 and EC135 from Airbus Helicopters (see Fig. 5). They are considered unmodified production rotorcraft in terms of aerodynamics, except for a noseboom attached to the EC135. The characteristics of both helicopters and their main rotors (MR) are summarized in Table 1. The CTA-measured wake velocities will be nondimensionalized using the rotors' hover-induced velocity,

$$V_h = V_{\text{tip}}\sqrt{\frac{C_T}{2}} = \sqrt{\frac{mg}{2\rho\pi R^2}} \tag{4}$$

The gross weight, mg, is used as a substitute for the rotor thrust, which is valid for hover-like conditions when neglecting the additional fuselage download. The helicopters started each test flight approximately with maximum takeoff mass, and the actual gross mass m for each test point during the flight was linearly interpolated using the elapsed time and the total fuel consumption measured after landing. The resulting ranges for m and V_h are stated in Table 1.

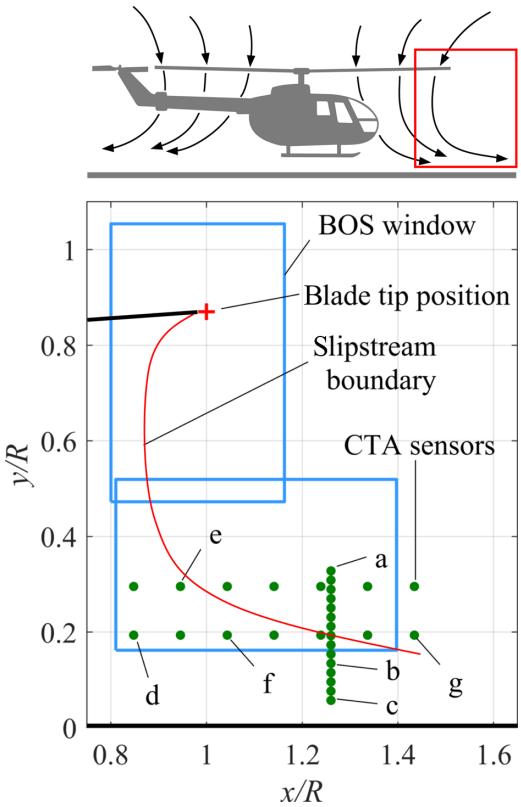

Fig. 7. Test geometry for Bo105 hover reference.

Results

Hover test cases

Bo105 reference flow field. This section discusses a Bo105 hover reference case as shown in Fig. 7. The average rotor hub position is $h = y/R = 0.83$ above ground, with the blade tip (+) being about $\Delta h = 0.045$ (0.22 m) higher due to blade coning. The horizontal axis was shifted so that the blade tip is at an average of $x/R = 1$. The BOS regions (—) and the CTA sensor positions (•) are sketched in relation to the rotor. Comparing different hover cases, the fixed BOS and CTA coordinates move relative to the rotor depending on the longitudinal position of the helicopter.

The time-averaged CTA velocity, V, in the x, y-plane for this reference case (▶) is shown in Fig. 8. The horizontal and vertical sensor array layouts were measured separately, but for the same hub height

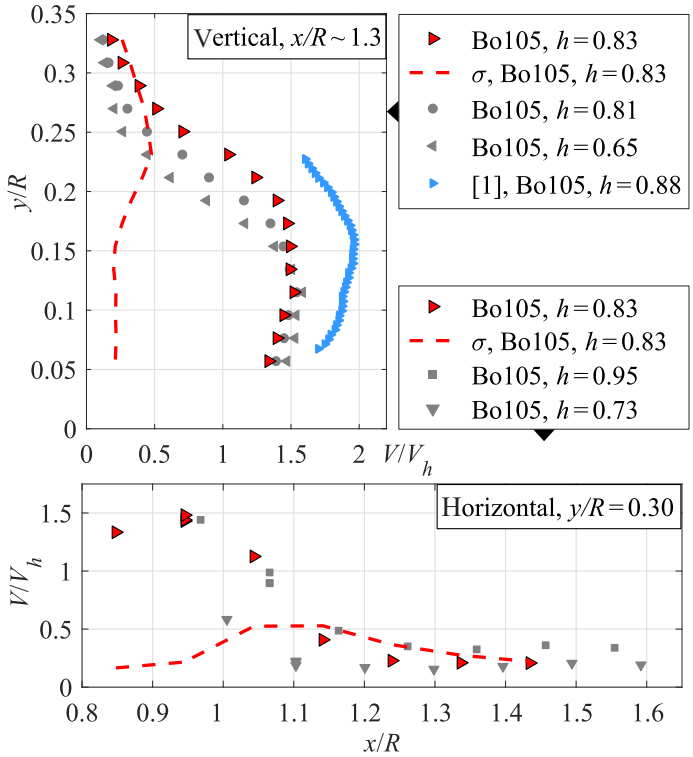

Fig. 8. Velocity profiles, hover test cases, including data from Ref. 1.

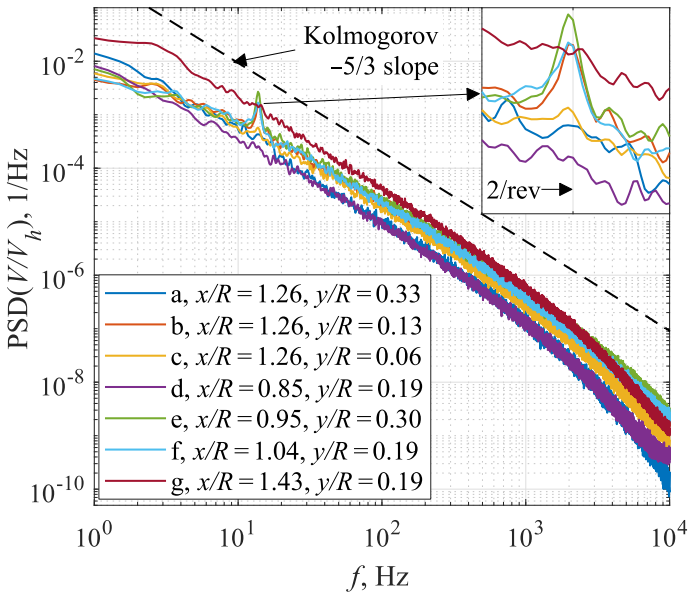

Fig. 9. Velocity spectra of CTA sensors a–g (see Fig. 7) for Bo105 hover case.

of $h = 0.83$ and similar environmental conditions. Data were only accepted if the helicopter was within a box of $\pm 0.04R$ around the stated average x, y-position. The vertical profile at $x/R = 1.3$ (Fig. 8 (top)) illustrates the development of a jet flow with a maximum velocity of 1.5 V_h at about $y/R = 0.13$–0.15 above ground. The peak value of the velocity's standard deviation σ (– –) is about 0.5 V_h, and it occurs in the area of the largest velocity gradient, at $y/R = 0.23$–0.25. A lower hub height squeezes the velocity profile closer to the ground, as seen for $h = 0.81$ (●) and $h = 0.65$ (◀). Figure 8 (top) also includes results by Schwarz et al. (Ref. 1). The three-component PIV data were re-evaluated in correspondence to the current CTA measurements: The average of $V = \sqrt{u^2 + v^2}$ (▶) is about 6% larger than the average of u as shown in the original publication, due to the additional v-velocity. The general shape of the profile agrees well to the current results, but it is offset by about 0.5 V_h. It will be shown later that this unexpected deviation is within the uncertainties introduced by the environmental wind conditions.

The horizontal profile along $y/R = 0.30$ (Fig. 8 (bottom)) shows that only the three innermost sensors are within the high-velocity rotor flow, $V > V_h$. For larger radii, $x/R > 1.1$, the velocity levels sharply decrease below 0.5 V_h in regions outboard of the rotor wake. The measured velocity distributions support the sketch of the wake boundary (—) suggested in Fig. 7.

Spectral analysis. The power spectral density (PSD) of the velocity signals was calculated using Welch's method (Ref. 47) with a frequency resolution of $\Delta f = 0.25$ Hz. The Welch algorithm calculates short–term Fourier spectra over windowed sub–parts of the signal which are then averaged. Figure 9 shows the spectral results for the Bo105 hover reference and a subgroup of CTA sensors on double–logarithmic scales. The PSD levels originate from aerodynamics, since they exceed the noise floor of the CTA system, as seen by measurements in quiescent air, in the chosen frequency range. The individual spectra are very similar despite being located in different areas of the flow (also see the corresponding labels **a** to **g** in Figs. 7 and 9). The slopes of all spectra are in good agreement to Kolmogorov's well-known -5/3 law (– –), at least over large parts of the frequency range, with an increasing overall PSD level corresponding to an increasing local standard deviation of the velocity. On top of this broad-banded signal, only the spectra **b** (—), **e** (—), and **f** (—) show small isolated peaks at a frequency corresponding to 2/rev, about 14 Hz. This result is unexpected for a four-bladed rotor implying a 4/rev periodicity at about 28 Hz. It is noted that the corresponding CTA sensors **b**, **e**, **f** are located along or slightly inboard of the wake's slipstream boundary, which indicates an involvement of the blade tip vortices convecting along this line.

A representative BOS snapshot of the Bo105 hover reference case, shown in Fig. 10 (left), gives further insight into the 2/rev phenomenon. The data are the scalar divergence of the BOS background shift, with dark areas corresponding to the low-density vortex core regions. The magnitude is arbitrary, since the system was not calibrated for quantitative measurements. One of the rotor blades points in forward direction at an azimuth of $\Psi \approx 180°$, and its contour was masked with a black line. The blade sheds the corresponding blade tip vortex I on a circular path, which projects onto an elliptical arc in the image plane of the BOS cameras. The preceding tip vortices II, III, IV, and V have been convected in downstream direction, and the corresponding wake ages are $\Psi_V = 90°$, $180°$, $270°$, and $360°$ at the foremost point of the vortex filament. Due to the camera perspective looking slightly upwards and due to the rotors turning counterclockwise when viewed from above, the upper branch of each filament belongs to the advancing side of the rotor plane, $\Psi = 0$–$180°$. It is noted that the current conventions, particularly a rotor blade pointing forward and the roman numbering of successive tip vortices, are continued throughout the paper if applicable.

The images also partly visualize the blade shear layers. For example, a faintly darker "mirrored S"-shaped structure stretches between vortices II and III, resulting from the blade shear layer II overtaking the tip vortex III due to its larger convection speed, as also shown in Refs. 2 and 48.

Label VI in Fig. 10 (left) marks remnant vortex filaments after a pairing between the two tip vortices aged $\Psi_V = 450°$ and $\Psi_V = 540°$.

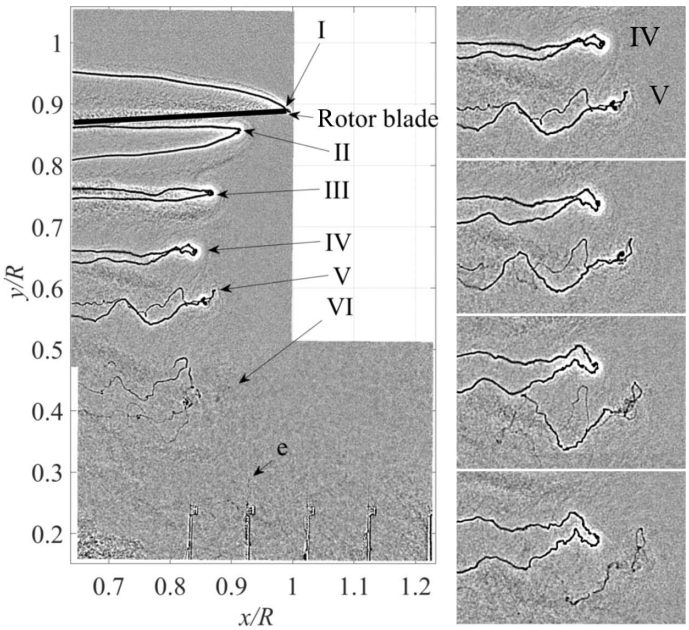

Fig. 10. Sample BOS result for Bo105 hover at $h = 0.83$ (left), detail of the pairing process between vortices IV and V over $\Delta t = 35.7$ ms (right).

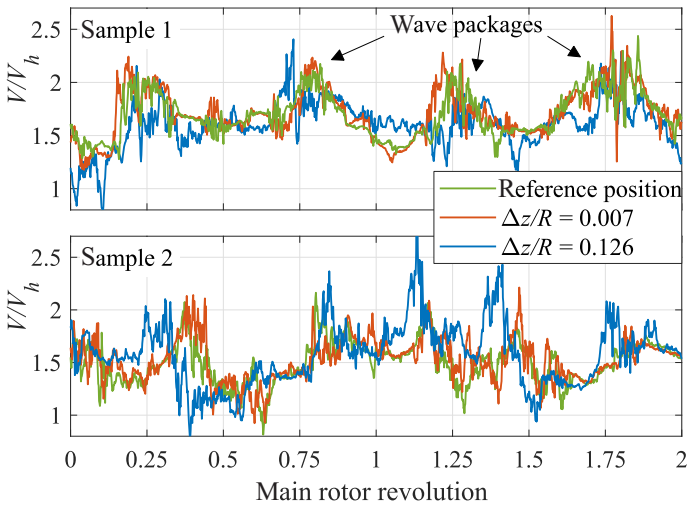

Fig. 11. CTA velocity samples at $x/R = 0.95$, $y/R = 0.30$, Bo105 hover.

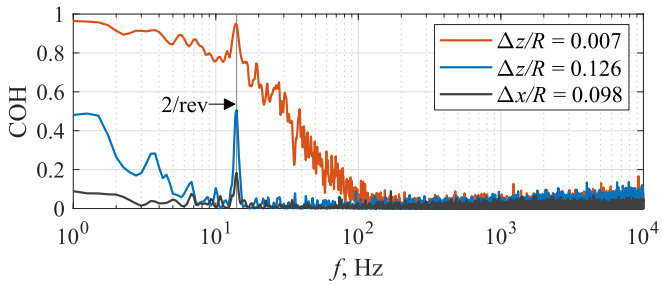

Fig. 12. Pairwise coherence of the CTA velocity with reference to $x/R = 0.95$, $y/R = 0.30$, Bo105 hover.

Vortex pairing is a frequent and repeatable process observed in the Bo105 hover cases, as shown in Fig. 10 (right) for the subsequent tip vortices IV and V in a time series covering a total of $\Delta t = 35.7$ ms or $\Delta\Psi_V = 90°$. The pairing involves a convergence and an orbital motion of both vortices around each other, which may lead to a reversed order ("leapfrogging") or even to vortex merging. The process is accompanied by instabilities, that is, deflections and bending of the vortex filaments. As a result, the earlier vortex V dissolves below the detection limit of the BOS system even before the pairing is fully finished. However, the resulting 2/rev periodicity persists in the wake flow, as shown by the CTA velocity spectra in Fig. 9. Vortex pairing has also been detected by Schwarz et al. (Ref. 1), and in other rotor studies (Refs. 21, 49–51). It can be related to small initial perturbations of the vortex spacing (see Bolnot et al. (Ref. 52)), which can result from differences in the tracking of individual blades.

Velocity signals and spatial coherence. The CTA sensor at position **e** (see Fig. 7, $x/R = 0.95$, $y/R = 0.30$) was complemented by two additional sensors staggered in the z-direction, which approximately matches the circumferential direction of the rotor, to further investigate the structure of the wake's slipstream boundary. The distances to the reference CTA position are $\Delta z/R = 0.007$ (0.035 m) and $\Delta z/R = 0.126$ (0.620 m), respectively. Figure 11 shows two short-term velocity samples taken from the same Bo105 hover case, with each sample covering two main rotor revolutions, in total about $\Delta t = 0.28$ s.

The signals with the small sensor spacing (— and —) agree well except for high-frequency content, whereas the correlation for the large spacing (— and —) is much lower. The first sample (Fig. 11, top) was chosen since it visually represents the 2/rev content by means of four successive wave packages evenly spaced over two revolutions. The 2/rev events appear as areas with a higher local velocity fluctuation due to the pairing and instability processes of the involved tip vortices. A comparison to the time-synchronous BOS data is difficult, since the trace of the tip vortices drops below the BOS detection limit before reaching the CTA sensors (Fig. 10). However, inspecting the corresponding BOS sequence and extrapolating the vortex tracks supports their relation to the velocity wave packages. The 2/rev periodicity is representative but not continuously observed over larger time spans of several seconds or minutes, which can be seen from the second sample of the same case (Fig. 11, bottom) or time-resolved representations of the power spectrum (not shown). This is due to aperiodic variations of the wake and a varying slipstream boundary position in relation to the fixed CTA sensors, as will be shown in the next section.

The velocity signals of the current hover case, about 120 s in total, were used to calculate the coherence function, COH. The COH is defined as the magnitude-squared cross–PSD of a pair of signals, divided by the product of the respective auto-PSD. The result is the level of signal correlation over the frequency and on a normalized scale between 0 and 1 (see Fig. 12).

The small Δz-spacing (—) results in a high coherence (COH $\geq$0.8) at low frequencies and a local peak (COH = 0.95) at the 2/rev frequency. The signals then successively loose coherence with increasing frequency and become uncorrelated (COH $\approx$0) at $f \approx 100$ Hz ≈ 14/rev. The decreasing trend is expected in the light of a fixed sensor spacing distance and Taylor's hypothesis (Ref. 53), suggesting that higher frequencies correspond to smaller spatial structures and vice versa. The large Δz-spacing (—) results in mostly uncorrelated signals, except for very small frequencies below 1/rev, and except for a very prominent peak (COH = 0.5) at 2/rev. For comparison, Fig. 12 also features the coherence for a step of $\Delta x/R = 0.098$ (—), which corresponds to an offset in the rotor-radial direction. The 2/rev peak is also present but much less prominent

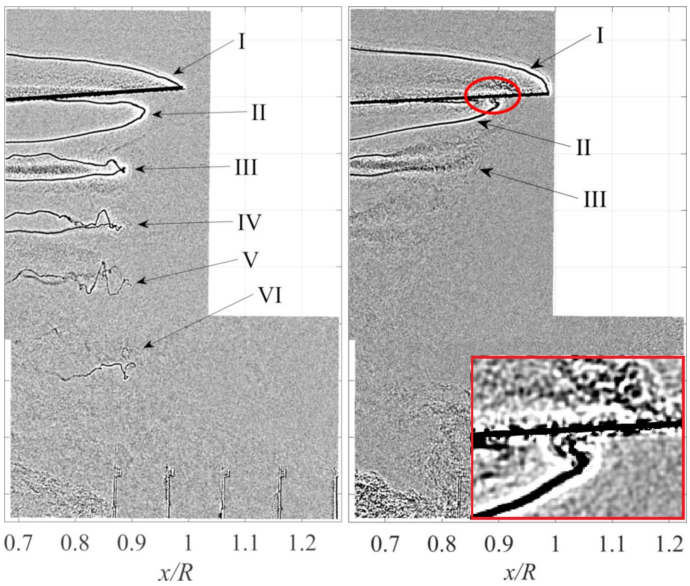

Fig. 13. Additional BOS sample results for Bo105 hover at $h = 0.83$, $V_{w,x} = -1.8$ m s^{-1}, same test as Fig. 10.

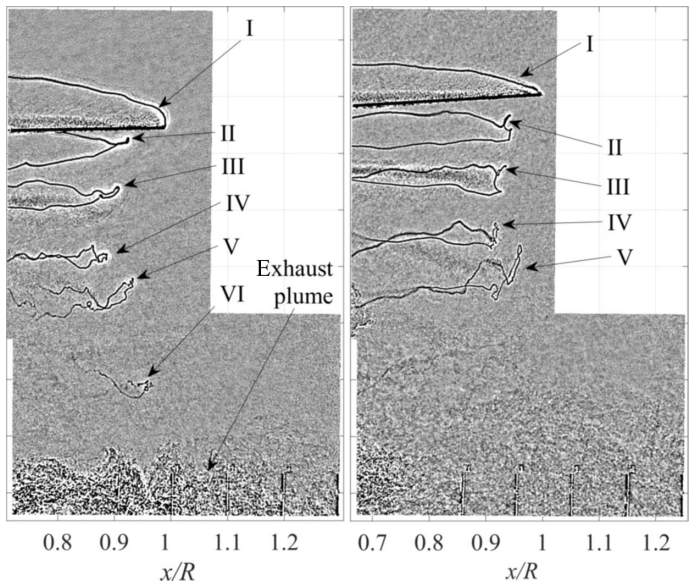

Fig. 14. BOS sample results for Bo105 hover at $h = 0.82$, $V_{w,x} = 0.9$ m s^{-1}.

(COH = 0.2). Hence, the 2/rev wave packages produce simultaneous fluctuations predominantly along the z-direction, meaning that the remnants of the tip vortices maintain their circumferential alignment after vortex pairing and instability processes.

Wind influence and comparison between Bo105 and EC135. The test campaign was conducted over several days in October 2019 and an influence of the prevailing wind conditions on the rotor wake could not be avoided. The Bo105 hover results in the preceding sections refer to test flights during which the local tower reported an average wind speed of 5.5 kn (2.8 m/s) from a direction of about $\Psi = 230^\circ$ (left-front) in the helicopter's azimuthal frame. This is slightly above Silva and Riser's (Ref. 17) 5 kn-limit for helicopter tests in quiescent air. The local wind condition in the test section was not measured; it will differ from the tower reading due to the atmospheric boundary layer and local obstacles such as the hangar. The tower data are nevertheless used to roughly categorize the different test points by means of the wind component in the x-direction, $V_{w,x}$. The Bo105 reference hover case yields headwind at $V_{w,x} = 2.8\,\text{m/s} \cdot \cos(230^\circ) = -1.8$ m/s. Figure 13 shows two additional BOS samples from this case. The left sample is qualitatively similar to the sample in Fig. 10, and both images were taken about 20 s apart but represent the bulk of the results in between. Again, the label VI marks a bundle of two tip vortices after pairing, whose trajectory hits the upper CTA sensor row at about $x/R = 0.9$–1.0.

The right sample in Fig. 13 shows a different and nonrepresentative wake layout from this test case, which is observed repetitively over several rotor revolutions spanning a total interval of about 2 s. The red framing marks an orthogonal BVI taking place at an azimuth of about $\Psi = 180^\circ$. The current rotor blade hits the preceding vortex II, which results in a dispersion of the vortex core, and which leads to a successive breakdown of the entire vortex filament from front to back. This development can be seen from the remnants of the older vortex III, which was also subject to BVI, and from the absence of any older tip vortices further downstream. Orthogonal BVI in the frontal area of the rotor plane can result from forward flight effects (see Tangler (Ref. 54)) and the flyover cases presented later in this paper. The current BVI pattern occurred while the helicopter remained in stationary hover, with very small longitudinal velocities $|V_x| < 0.15$ m/s. Therefore, it is assumed that the BVI was caused by a superposition of an average headwind component $V_{w,x}$ and an unsteady wind gust temporarily increasing the inflow velocity.

In contrast, Fig. 14 shows two BOS samples for a Bo105 hover case in a similar average hub height of $h = 0.82$, but with a slight tailwind condition as indicated by the tower, 4 kn from $\Psi = 295^\circ$ (left-rear), or $V_{w,x} = 0.9$ m/s. There are three consequent differences to the reference case: First, the wake boundary is pushed in the forward direction towards larger x-coordinates. For example, the extrapolated tip vortex trajectory now intersects the upper CTA sensors, $y/R = 0.3$, in the area of $x/R = 1.0$–1.1 instead of $x/R = 0.9$–1.0. Second, the changed wind condition results in the absence of any BVI event over the entire test interval. Third, a larger amount of exhaust gases is entrained into the BOS field of view. This can result in dense thermal schlieren clouds close to the ground, as in the left sample, or a generally higher noise level in the lower half of the BOS image, as in the right sample. Apart from these differences, the general structure of the wake is unchanged, including regular vortex pairing as seen for vortices IV and V in both samples of Fig. 14.

Hover tests with the EC135 helicopter were conducted with a larger tower-indicated tailwind component of $V_{w,x} = 4.6$ m/s. The rotor wake boundary is pushed further forward in the positive x-direction (see Fig. 15 for two representative BOS samples at an average hub height of $h = 0.78$). The biggest difference to the Bo105 results is that no vortex pairing is observed in the schlieren images. Instead, the spacing between subsequent vortices shed from different rotor blades remains rather equidistant within BOS detection boundaries. This not only holds true for the shown samples, but it is a general characteristic for the current EC135 tests with very few exceptions. Individual vortex filaments still develop long-wave deflections and subsequent noncooperative instabilities initiating vortex breakdown. The maximum detectable vortex age is slightly larger than for the Bo105 and in the range of $\Psi_V = 540^\circ$–630°, represented by vortices VI and VII in Fig. 15. The noseboom of the test rotorcraft partly obstructs the vortex trajectories, seeding additional instabilities.

For helical vortices, initial spacing perturbations as low as 1% of the average vortex separation distance are known to be amplified and yield

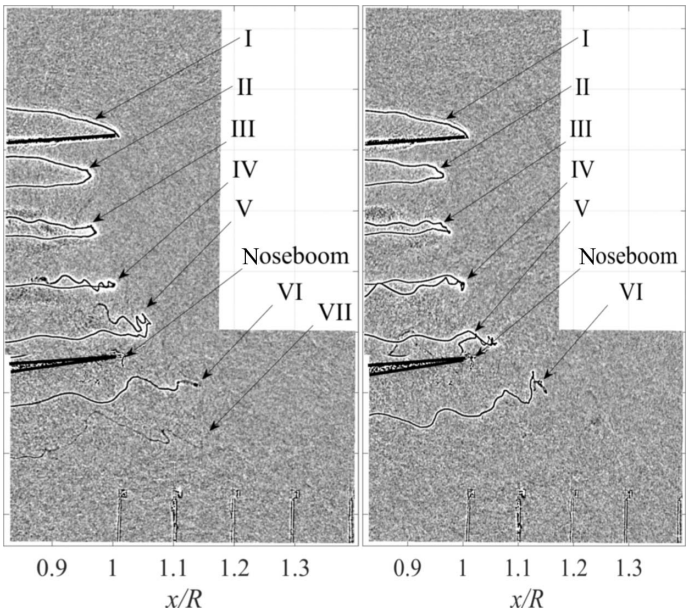

Fig. 15. BOS sample results for EC135 hover at $h = 0.78$, $V_{w,x} = 4.6$ m s^{-1}.

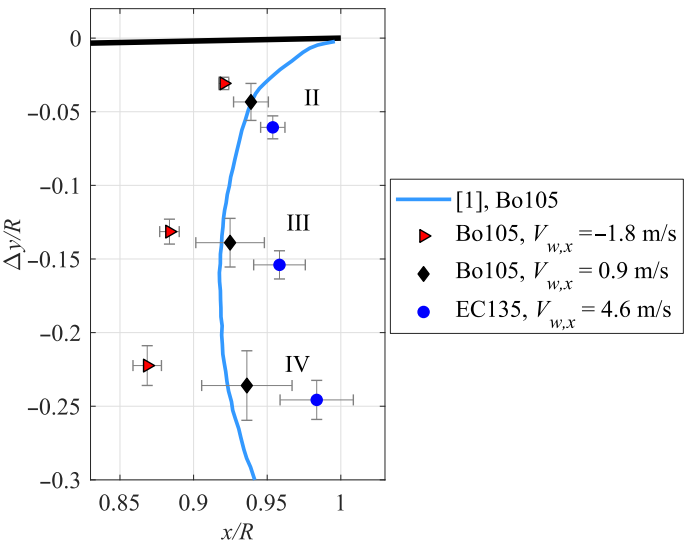

Fig. 16. Tip vortex trajectories for vortex ages $\Psi_V = 90°, 180°, 270°$ (II, III, IV) and data from Ref. 1.

pairing after only a few revolutions (see Ref. 52). Hence, a reproducible pairing can be triggered by differences in the tracking of individual rotor blades, which in turn leads to systematic differences of the tip vortex trajectories as also noted by Ref. 1. The rotors of both current aircraft were tracked by the DLR maintenance facilities using the same standard optical system of type "Honeywell Chadwick VXP." The EC135 indeed showed smaller blade track height differences than the Bo105 in both IGE hover, 1 mm versus 4 mm, and maximum level flight speed, 5 mm versus 11 mm.

The conclusions of the individual BOS snapshots are supported by statistics. Figure 16 shows the average positions of vortex ages $\Psi_V = 90°$, 180°, and 270° (II, III, and IV) in relation to the blade tip position at $x/R = 1$ and $\Delta y = 0$. The results were averaged over more than 200 samples covering all four rotor blades and the entire time span of each

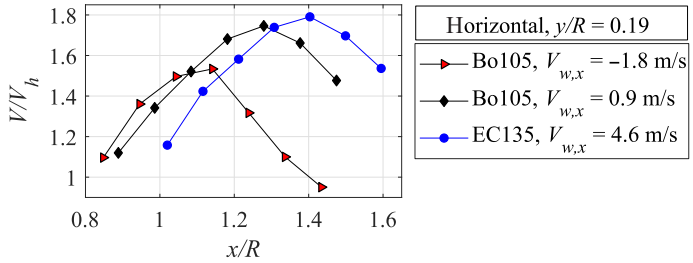

Fig. 17. Horizontal velocity profiles, hover, corresponding to the BOS results in Figs. 13 to 15.

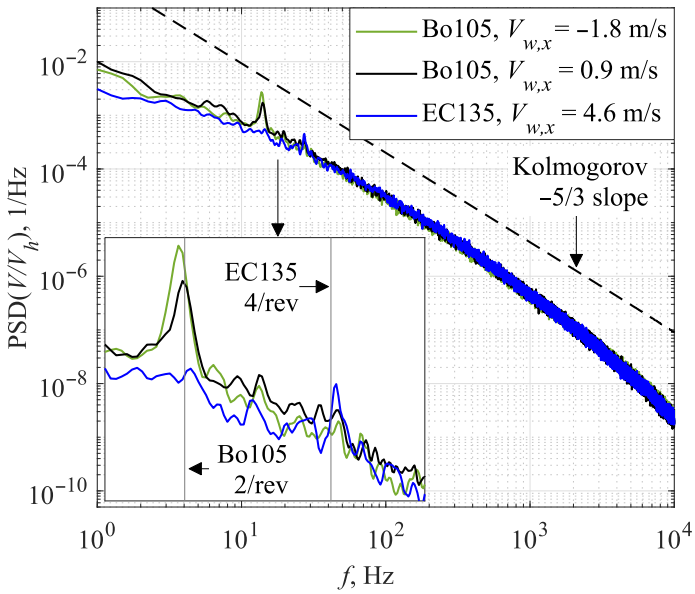

Fig. 18. Velocity spectra in the slipstream boundary, hover, Bo105 and EC135, corresponding to Figs. 13–15.

test run, about 20 s. The vortex trajectories of former IGE tests with a Bo105 rotorcraft (—, Ref. 1) were added as references.

The statistics show a systematic correlation between the tip vortex trajectories and the tower-indicated wind component $V_{w,x}$, representing the influence of the local wind on the rotor wake's shape and slipstream boundary. Therefore, quantitative comparisons of full-scale test campaigns in outdoor conditions require particular caution. It is noted that the current trajectory for $V_{w,x} = 0.9$ m/s is similar to but slightly outboard of the preceding DLR PIV study for the Bo105 (—), indicating that Schwarz et al. measured under more or less quiescent conditions.

The current test with a headwind component (▶, $V_{w,x} = -1.8$ m/s) notably reduces the miss distance between the forward-pointing rotor blade and the preceding tip vortex at $\Psi_V = 90°$, increasing the possibility of orthogonal BVI in this area. The vortex spacing distances of Bo105 (▶, ♦) and EC135 (●) cases are similar but slightly larger in the latter case. In addition to the wind differences, the EC135 has a 10% increase in V_h and a 7% reduction in rotor speed over the Bo105 (Table 1), which amplifies streamwise vortex separation. On the other hand, the EC135's larger twist reduces the local downwash in the tip area for a given V_h.

Figure 17 shows the average velocity profiles measured in the horizontal direction, $y/R = 0.19$, for the different test cases of Figs. 13–16. Comparing both Bo105 cases (▶,♦), a larger value of $V_{w,x}$ increases both the strength and the x-coordinate of the velocity maximum. The outboard displacement of the wake's slipstream boundary (Fig. 16) and

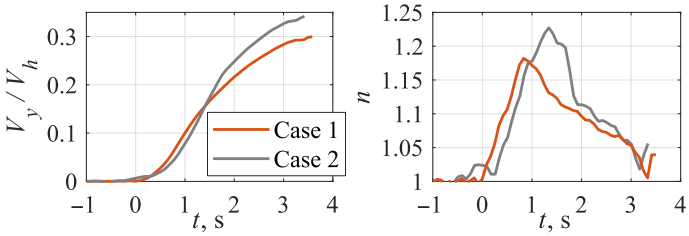

Fig. 19. Vertical velocity (left) and load factor (right) for sample vertical takeoff cases.

the shifting velocity peak position (Fig. 17) are consistent, and this trend is continued by the EC135 case (•) with an even larger tailwind.

Figure 18 shows velocity spectra of individual CTA sensors for the three conditions and at $y/R = 0.3$. The x locations were chosen so that each sensor is slightly inboard of the slipstream boundary, corresponding to label **e** in Fig. 7.

For this sensor choice, the velocity spectra of the different wind conditions and helicopters are nearly coincidental and, again, comply to Kolmogorov's -5/3 law. The only notable difference is connected to the vortex pairing phenomenon, which results in distinct peaks with a 2/rev periodicity for both Bo105 cases (— and —) regardless of the wind condition. In contrast, the EC135 case (—) is void of a 2/rev peak but instead exhibits a smaller peak at the 4/rev periodicity. This peak was expected on the basis of the schlieren results and complies to the evenly spaced EC135 tip vortices of all four rotor blades (also see the BOS samples in Fig. 15).

Vertical takeoff test case

Schwarz et al. (Ref. 1) already investigated vertical takeoff test cases with DLR's Bo105 helicopter and concluded that the tip vortex trajectories are similar to hover, but the maximum detectable vortex age is slightly larger as a consequence of the increased thrust level. However, a rapid execution of the maneuvers was impaired by the pilots wearing laser safety goggles at night to enable PIV measurements, which is not required in the current case. The current maneuvers were also conducted with the Bo105, similar tests with EC135 showed that the heavier rotorcraft is less agile and its noseboom is very close to the CTA array when taking off from the ground. The Bo105 was setup in reference position, similar to the EC135 in Fig. 1 but with the skid on the ground. Starting with a neutral collective blade pitch and approximately zero lift, the pilots then took off as fast as possible. Figure 19 shows the vertical velocity, V_y, and the corresponding load factor, n, for two sample maneuvers, case 1 (—) and case 2 (—). The experiments were conducted under a tower-indicated wind component of $V_{w,x} = -1.8$ m/s.

The time axis was shifted so that $t = 0$ corresponds to takeoff, and the helicopter left the position tracking window with a vertical velocity, V_y, exceeding 3.2 m/s or 0.3 V_h. The peak load factor, n, is 1.18 and 1.23, respectively, indicating a corresponding thrust increase over hover conditions (Schwarz et al.: 1.04). Maintaining a perfectly vertical flight path is difficult, and the helicopters drifted slightly backwards during the maneuver (case 1: $\Delta x = -0.7\ m$, case 2: $\Delta x = -0.4\ m$). Both pitch and yaw angle showed oscillations bounded by $\pm 6^\circ$.

Figure 20 shows CTA velocity signals of the upper horizontal array sensor row, located at three different radial positions. The innermost sensor, $x/R = 0.87$ (a), responds to the collective control input and the increasing wake velocity before takeoff, $-5\ \text{s} < t \leq 0$. The same holds true for the central sensor at $x/R = 0.97$ (b), which is located in the slipstream boundary and, therefore, has a much larger fluctuation level.

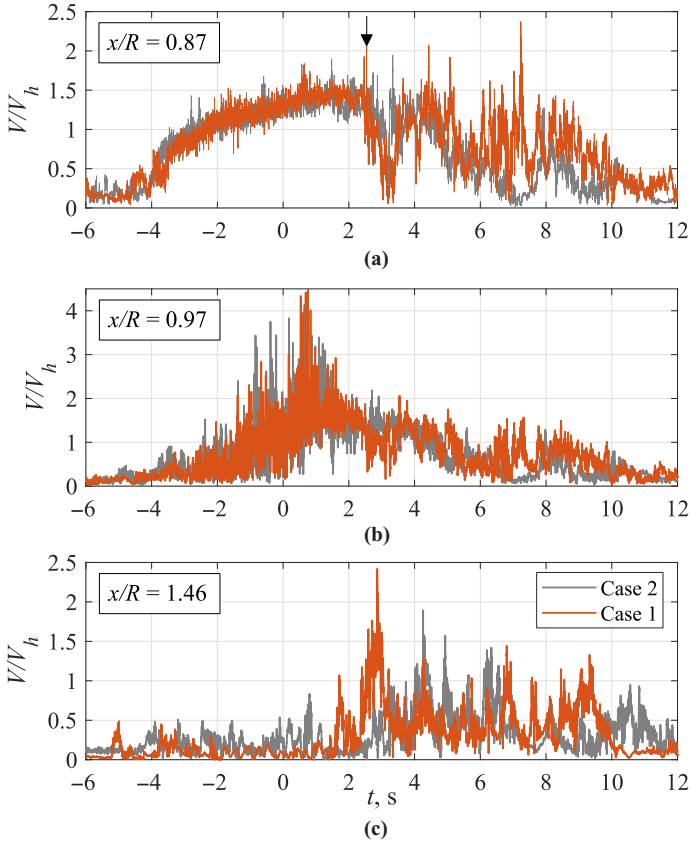

Fig. 20. CTA velocity signals for takeoff cases 1 and 2 at $y/R = 0.3$ (upper row) and different radial positions.

The outermost sensor at $x/R = 1.47$ (c) is located above the outwash flow and measures very small velocities in the early part of the maneuver. Up to this point, the results correspond to the hover profiles (e.g., see Fig. 8).

The trend is continued after takeoff and up to about $t = 2.7$ s (see the black arrow marker in Fig. 20(a)). At this point, the hub is at $y = 6.8\ m$ or $h = 1.39$, well above the schlieren field of view and the hover test cases discussed in the preceding section. The structure of the velocity signals significantly changes, and the sensors at $x/R = 0.87$ and 0.97 no longer reflect the characteristic footprint of the wake and the slipstream boundary. All three radial positions are subject to high-amplitude low-frequency oscillations, which indicate large-scale instability effects close to the ground. The velocity levels trail off after about $t = 12$ s. Both test cases 1 and 2 agree well in terms of their general characteristics, and the two innermost signals of case 1 (—) are further analyzed in Fig. 21 by means of time-resolved spectrograms. The Welch spectrum approach was used, but the individual short-term spectra were assigned to their corresponding points in time, t, rather than time-averaged. The coloring corresponds to the same logarithmic scaling of the PSD (see Figs. 9 and 18).

The rotor harmonics are present between $-5\ \text{s} < t \leq 2.7$ s, which particularly covers the Bo105's vortex pairing-related excitation of a 2/rev periodicity visible in the wake flow (Fig. 21(a)). The 4/rev also shows slightly increased PSD levels, probably since the pairing is not always entirely finished for low hub heights. Within the area of the slipstream boundary (Fig. 21(b)), the rotor harmonics are superimposed with broad-banded turbulent fluctuations. The structural change of the wake for $t > 2.7$ s is characterized by an excitation of low-frequency

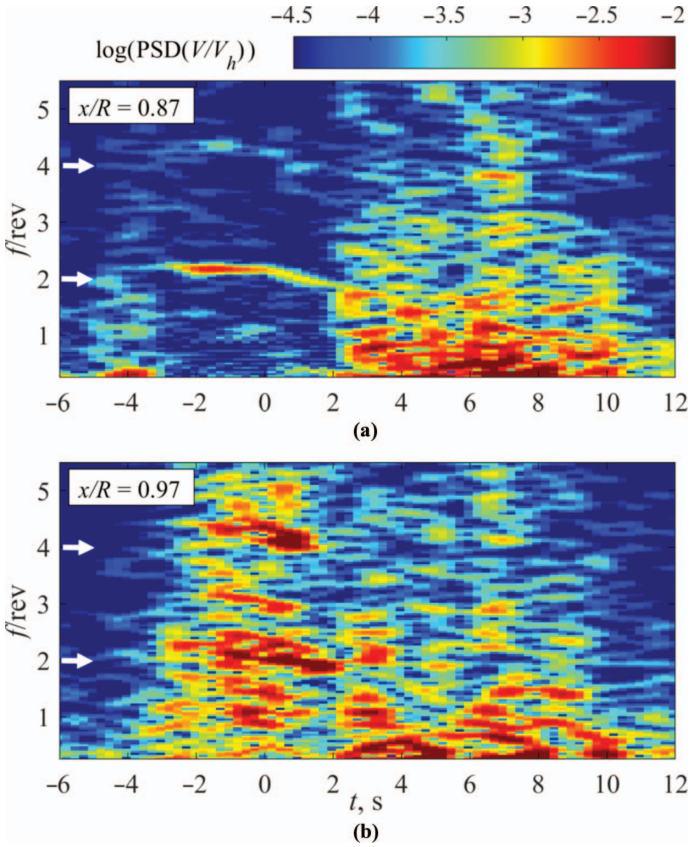

Fig. 21. Spectrograms for Bo105 takeoff case 1 in Figs. 20(a) and 20(b).

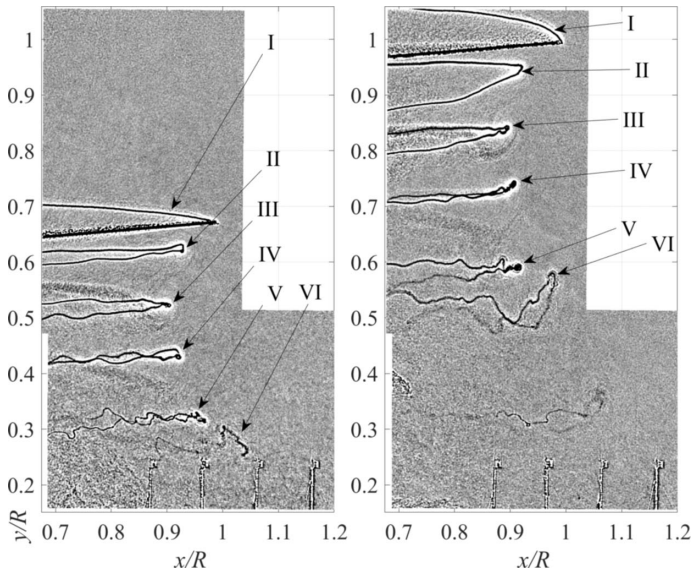

Fig. 22. BOS sample results for Bo105 takeoff case 1 at $t = 0.74$ s (left) and $t = 1.76$ s (right).

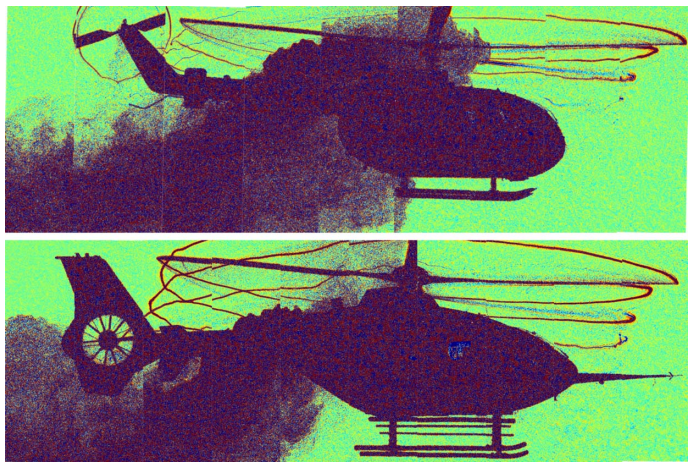

Fig. 23. Compilations of schlieren images for forward flight cases, Bo105 (top, $h = 0.89$, $\mu^* = 0.47$, $V_x = 5.1$ m s^{-1}) and EC135 (bottom, $h = 0.87$, $\mu^* = 0.76$, $V_x = 9.1$ m s^{-1}). One of the main rotor blades points forward at $\Psi \approx 180°$.

oscillations well below 2/rev. In this timespan, the velocity signals at $x/R = 0.87$ and 0.97 are highly correlated, COH > 0.5 for $f < 3$ Hz, underlining the structure of large-scale fluctuations.

The systematic occurrence of tip vortex pairing during Bo105 takeoff is reflected by two BOS snapshots for $h = 0.61$ at $t = 0.74$ s (Fig. 22 (left)) and for $h = 0.92$ at $t = 1.76$ s (Fig. 22 (right)). It is noted that the takeoff pairing occurs slightly later, between $\Psi_V = 360°$ and $\Psi_V = 450°$ (V and VI), compared to the hover cases with pairing ages usually between $\Psi_V = 270°$ and $\Psi_V = 360°$ (IV and V in Figs. 10 and 14). This delay can result from the increased convection velocity at high takeoff thrust levels with $n > 1$. For the large-scale turbulent wake state, $t > 2.7$ s, the BOS results (not shown) only detect some smaller incoherent remnants of the tip vortices close to the top of the measurement field, but no vortical structures close to the ground.

Forward flight-test cases

Forward flight tests were conducted with the CTA sensors in the horizontal array configuration and with both the Bo105 and EC135 rotorcraft. The pilots aligned the helicopters along the global x-axis while hovering about 80 m in front of the test setup. They then accelerated to predefined flight velocities, V_x, between 3 and 11 m/s as indicated by an on-board GPS speed meter and maintained a steady level flight as well as possible. Invalid test runs were sorted out during the post-processing on the basis of the SPR position and velocity data. At the maximum velocity of 11 m/s, the fuselages of both rotorcraft were pitched down at angles between 7° and 9° compared to the hover cases. The pilots tried to fly as low as possible while not colliding with the sensor array. A slightly larger hub height, about $0.8 < h < 1.1$, was required in comparison to the hover cases due to safety considerations. Also, the available amount of measurement data is relatively small since the helicopters quickly traverse the test section, so each condition was repeated between one and three times.

Figure 23 shows an overview of the Bo105 (top) and EC135 (bottom) in forward flight. The figures were compiled by merging 10 individual BOS images during which the helicopters moved through the field of view, creating a scanning effect. The azimuth of the main rotor is approximately the same in all images, but some discontinuities appear at the image seams due to wake aperiodicities and the asynchronously fixed camera frequency. The figure shows the usual scalar BOS signal defined in Eq. (3), which was mapped in false colors to increase the contrast of the fuselage. The helicopter structure blocks the background pattern, resulting in random noise (dark colors) when correlated with the reference image. Due to the small interrogation windows, this effectively

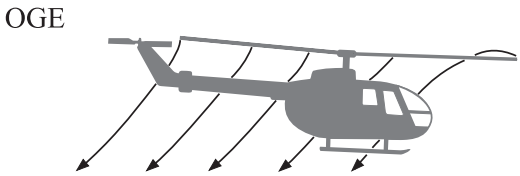

Fig. 24. Wake in forward flight, OGE (after Ref. 35).

masks even fine details such as the skid or the fenestron blades without further post-processing. The exhaust gas of the engines creates thermal schlieren, which visualize the outline of the plume but mask any further structures in this area. The rotor wake and its vortical structure is visible in the areas over the bow, $\Psi \approx 180°$, and over the tail, $\Psi \approx 0°$.

Velocity signals. The transition from hover into forward flight changes the layout of the rotor wake and introduces a wake skew angle, which is sketched in Fig. 24 for outside ground effect (OGE) conditions. The presence of a ground surface, IGE, adds further flow structures depending on the normalized advance ratio $\mu^* = V_x/V_h$. The following categorization is based on the results by Sheridan and Wiesner (Ref. 24) and Curtiss et al. (Ref. 25) for a hub height of about $h = 0.8$–1.0.

The flow around the helicopter remains "hover-like" up to $\mu^* = 0.4$, with a small recirculation system forming way ahead of the rotor (see Fig. 25(a)). This vortical structure grows in size and moves closer to the helicopter in the "recirculation regime," $0.4 < \mu^* \leq 0.7$, as sketched in Fig. 25(b). A further increase of the helicopter's velocity causes the vortex to move under the rotor plane, with a center located between the bow and the blade tip radius (see Fig. 25(c)). The corresponding "ground vortex regime" stretches between $0.7 < \mu^* \leq 0.9$. The ground vortex disappears for $\mu^* > 0.9$ (see Fig. 25(d)) and is replaced by a flow field similar to OGE conditions, indicating a reduced influence of the ground surface on the flow pattern ahead of the helicopter.

Figure 26 shows the CTA velocity signals for Bo105 forward flight-test points, with different advance ratios corresponding to the four different flow regimes, and with hub heights between $h = 0.96$ and 1.02. The signals of the seven CTA sensors in the lower row at $y/R = 0.19$ (—) were time shifted so that $t = 0$ is when the rotor hub passes the x-position of each individual sensor. Additionally, the data of all sensors was averaged in a sliding window sized $\Delta t = 0.5$ s (—).

The flow velocity V was measured in the nonmoving coordinate system and cannot be transferred into the moving helicopter frame, since this requires to determine the individual x, y-velocity components rather than the scalar in-plane velocity value V. Nevertheless, the different flow regimes can be clearly differentiated.

The hover-like wake of the lowest advance ratio, $\mu^* = 0.27$ in Fig. 26(a), results in a radial outwash flow ahead and behind of the helicopter. The velocity levels gradually trail off after about $t = 15$ s, but the shown detail for $-3 \text{ s} < t \leq 6$ s has a high average velocity in the range of 0.5 V_h to 1.2 V_h with a comparably high fluctuation level. There is a small velocity overshoot ahead of the rotor, 1.65 V_h at $t = -1.7$ s. For $-1 \text{ s} < t \leq 1$ s, the fuselage shields the sensor from the rotor wake, resulting in a low-velocity plateau. The formation of a recirculation vortex is noted at $\mu^* = 0.55$ (see Fig. 26(b)) by means of a distinct velocity peak between $-2.5 \text{ s} < t \leq 0.5$ s. The maximum average velocity of about 1.5 V_h is located at $t = -0.87$ s. When considering the helicopter's flight velocity of $V_x = 6.04$ m/s, this corresponds to a point $\Delta x/R = 1.07$ ahead of the hub center and, therefore, slightly outside the rotor radius. Again, the sensors are shielded by the fuselage, and the flow trails off after $t = 6$ s. The flow for $\mu^* = 0.80$ (see Fig. 26(c)) is qualitatively similar to $\mu^* = 0.55$ but squeezed into a shorter time frame. The peak of the average velocity before the passage of the fuselage is 1.75 V_h at $t = 0.28$ s, which corresponds to a point $\Delta x/R = 0.49$ ahead of the hub for $V_x = 8.65$ m/s. This shows that a ground vortex is now located under the rotor plane and within the rotor radius. The highest flight speed, $\mu^* = 1.19$ in Fig. 26(d), significantly alters the footprint by means of both lower average velocities and lower fluctuation levels and by the absence of a large-scale vortical structure in front of the helicopter. The rotor wake hits the CTA sensors at about $t = 0.1$ s, which is seen by a sudden increase of the velocity fluctuations at an average level of 0.7 V_h. This means that due to the wake skew, the rotor flow reaches the sensor positions slightly after the hub has passed. The flow is accelerated ahead of the wake boundary, $-1.0 \text{ s} < t \leq 0.1$ s, due to low-turbulent upstream entrainment effects, which is a unique and characteristic feature of this flight state.

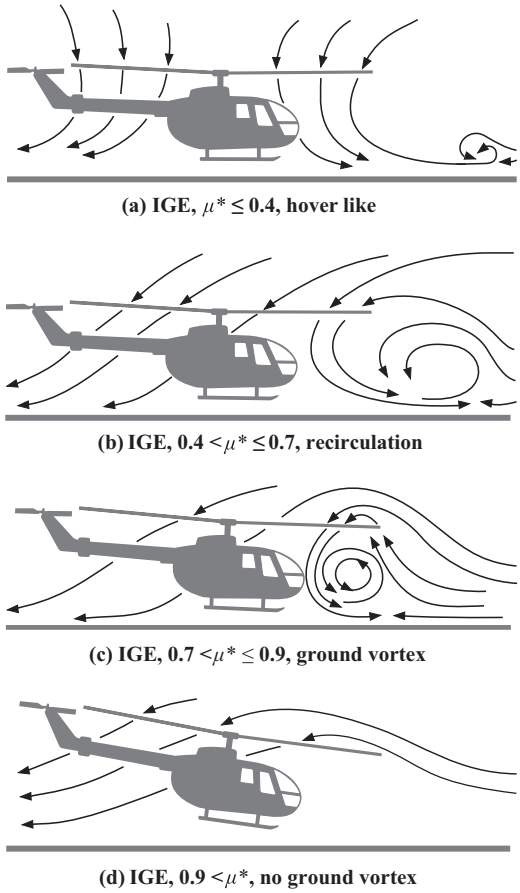

(a) IGE, $\mu^* \leq 0.4$, hover like

(b) IGE, $0.4 < \mu^* \leq 0.7$, recirculation

(c) IGE, $0.7 < \mu^* \leq 0.9$, ground vortex

(d) IGE, $0.9 < \mu^*$, no ground vortex

Fig. 25. Wake in forward flight, IGE (after Refs. 24, 25).

Figure 27 shows the average CTA velocity footprint for four test runs in the "recirculation vortex" regime with comparable values for h and μ^*. The data from Fig. 26(b) are repeated as a reference (—), and the other cases cover both helicopters and different wind conditions. The large-scale features of the velocity footprint (recirculation vortex, fuselage shielding, and trailing wake) are consistently observed in all four cases, indicating that the general layout of the rotor wake is comparable. Nevertheless, the individual signals differ from each other by up to 0.25 V_h and show some smaller-scaled oscillations with wavelengths on the order of 1 s. The short measurement intervals and the large velocity fluctuations prevent a consistent interpretation of the different environmental conditions as conducted for the long-term hover measurements, for example, Fig. 17.

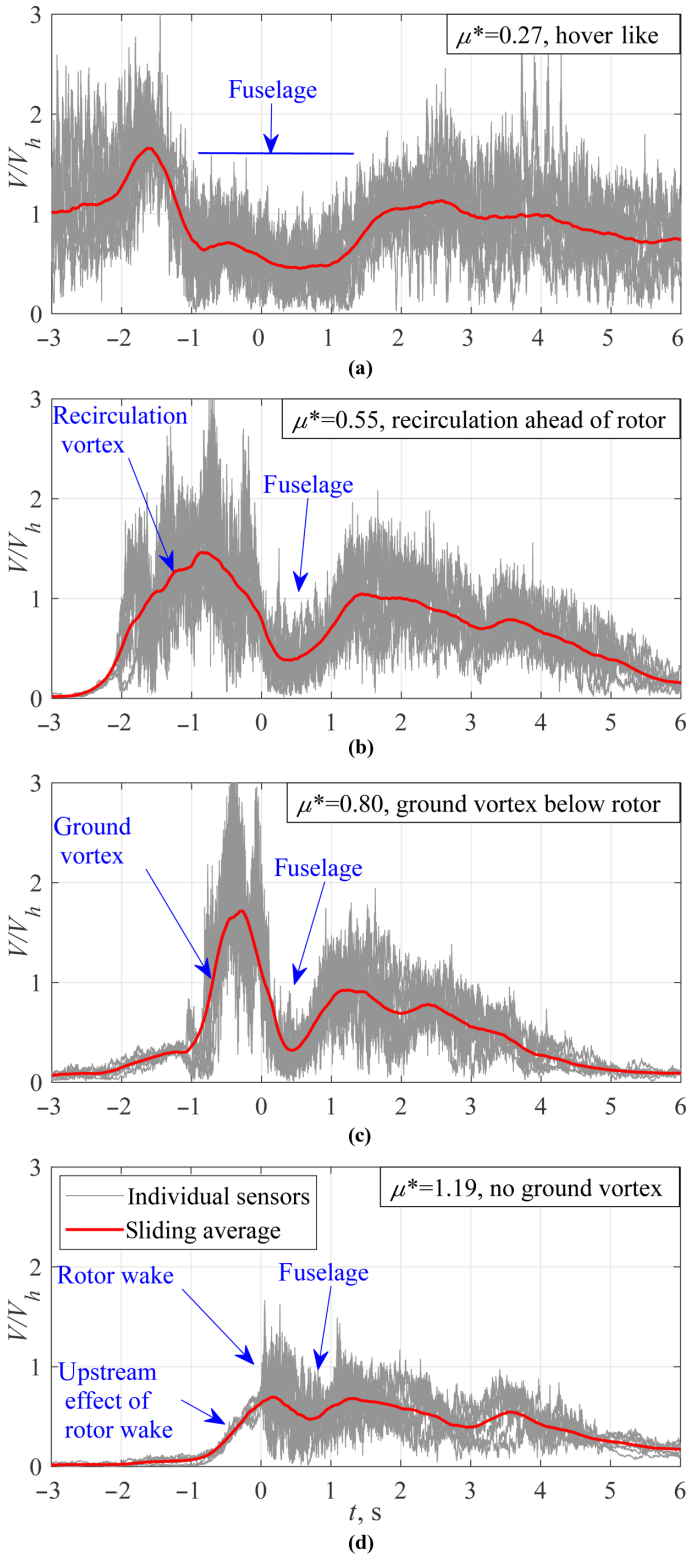

Fig. 26. CTA velocity signals at $y/R = 0.19$ for Bo105 forward flight at different normalized advance ratios μ^*.

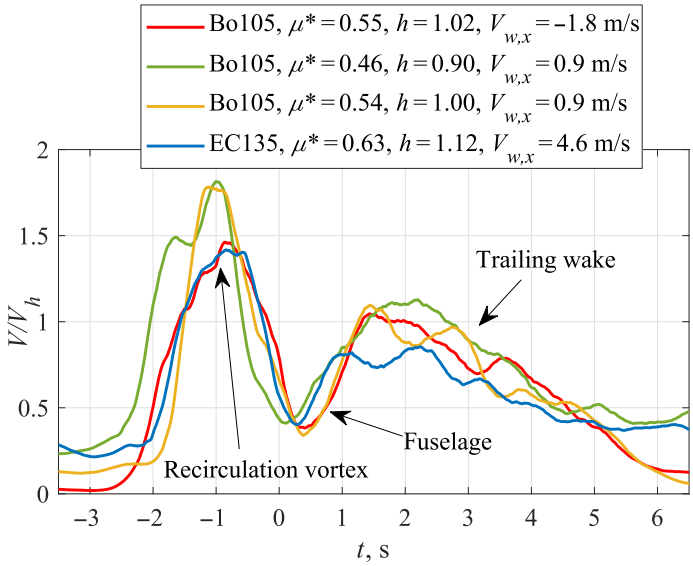

Fig. 27. Average CTA velocity signals at $y/R = 0.19$ for different test runs in the recirculation regime.

BVI of the main rotor. The schlieren results show BVI in the frontal part of the rotor plane due to forward flight effects and similar to the wind gust in Fig. 13 (right). Edgewise flight affects the velocity distribution through the rotor plane as predicted by inflow models for OGE conditions (e.g., see Chen (Ref. 55)). The longitudinal direction is modeled by a cosine term predicting an upwash component over the bow at $\Psi = 180°$. Depending on the wake skew and the advance ratio, this upwash term can be large enough that the flow direction in the tip area is reversed and points bottom to top, also see the sketch in Fig. 24. The ground effect further intensifies the upwash effect in the "ground vortex" regime, approximately $0.7 < \mu^* \leq 0.9$, due to the large vortical structure located under the rotor and in front of the bow (see Fig. 25(c)).

The upwash component affects the tip vortex trajectories, as shown in Fig. 28 for the Bo105 as a function of different normalized advance ratios μ^*. The coordinate system corresponds to the hover results with the rotor hub at $x = 0$ and the ground surface at $y = 0$, but the field of view was reduced to focus on the blade tip area only. Four of the six test cases ($\mu^* = 0.27, 0.55, 0.80, 1.19$) were already discussed by means of their velocity footprint in Fig. 26. For a small advance ratio of $\mu^* = 0.27$ (see Fig. 28(a)), the wake system is hover-like with a detectable vortex age up to $\Psi_V = 360°$ at label V, but the helicopter's forward motion increases the wake skew. In particular, the tip vortex II at an age of $\Psi_V = 90°$ is closer to the rotor plane but further inboard in comparison to the hover results (see Figs. 10 and 13). This trend intensifies when increasing μ^* to 0.55 (see Fig. 28(b)). Vortex II now almost touches the rotor plane, and the beginning interaction leads to faster breakdown of the subsequent vortex system. Vortex III has already dissipated, but some scattered and incoherent vortex filaments are visible at an age of about $\Psi_V = 270°$, label IV.

The blade exactly hits the preceding tip vortex when $\mu^* = 0.71$, as shown in Fig. 28(c), and the advancing-sided (upper) branch of vortex filament II was erased due to BVI. A further increase of the forward velocity and the connected upwash velocity lifts the tip vortex sheet above the rotor plane (see Figs. 28(d)–28(f)). At $\mu^* = 1.02$, vortex II is above the rotor plane and the rotor blade hits the vortex filament III at an age of $\Psi_V = 180°$. At $\mu^* = 1.19$, both vortices II and III are located above the rotor plane. Even though BVI is not visible in this image, an analysis of the schlieren image time series shows that the small miss distance between rotor blades and tip vortices induces disturbances, which cause vortex III to dissolve shortly after the shown time instant.

The results in Fig. 28 involve the Bo105 reference conditions with a tower-indicated headwind of $V_{w,x} = -1.8$ m/s. The corresponding hover analysis indicated a small miss distance between rotor blades

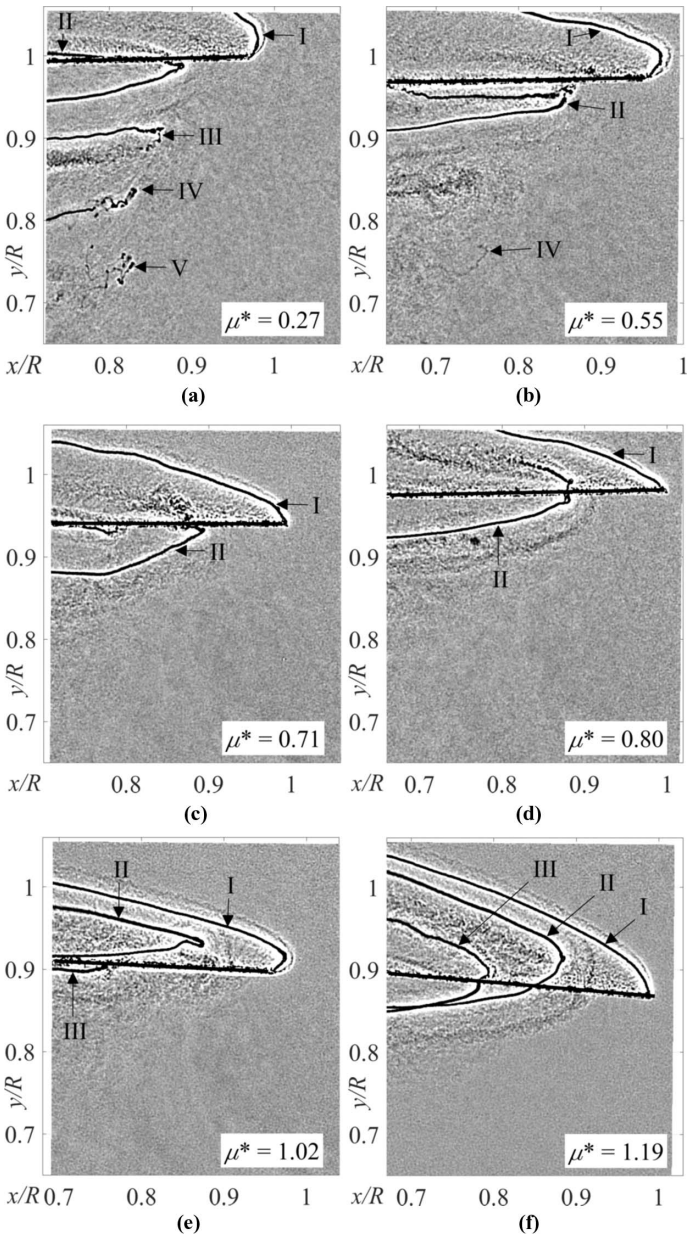

Fig. 28. BVI in the frontal region of the Bo105's MR plane for different advance ratios, $V_{w,x} = -1.8$ m s^{-1}.

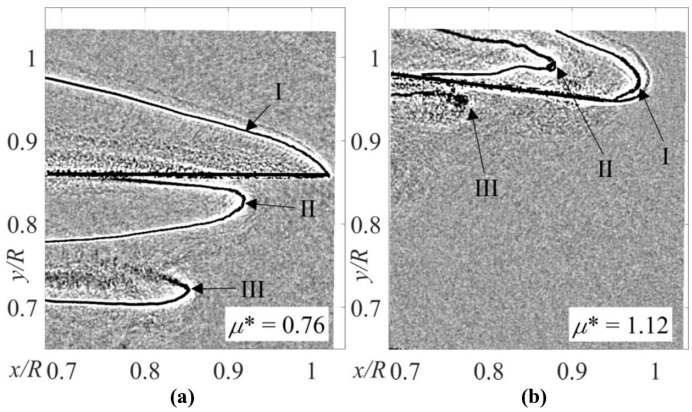

Fig. 29. BVI in the frontal region of the EC135's MR plane for different advance ratios, $V_{w,x} = 4.6$ m s^{-1}.

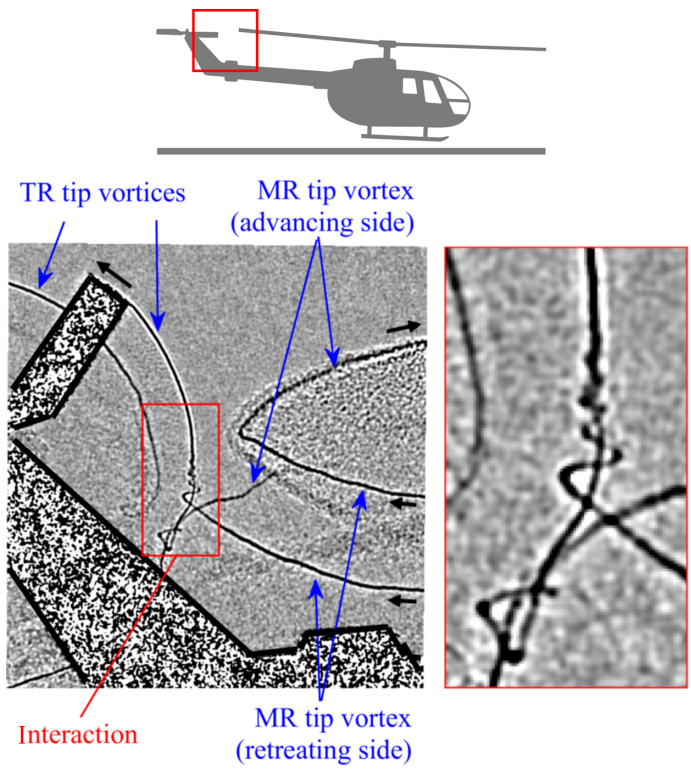

Fig. 30. Interaction between the tip vortices of Bo105's main rotor (MR) and tail rotor (TR), $\mu^* = 0.43$.

and tip vortices (see Fig. 16), which also implies an early start of BVI in forward flight. This is confirmed by a comparison to the largest miss distance, occurring for the EC135 during a tailwind of $V_{w,x} = -4.6$ m/s. The tip vortex system is still hover-like at $\mu^* = 0.76$ (see Fig. 29(a)), with vortices II and III located below the rotor plane. Vortex breakdown is noted on the advancing (upper) branch of vortex III. Increasing the normalized advance ratio to $\mu^* = 1.12$ (see Fig. 29(b)) yields BVI between the rotor blade and tip vortex III, with vortex II being located above the rotor plane. A strong qualitative resemblance to the Bo105 case at $\mu^* = 1.02$ in Fig. 28(e) is noted, indicating that the BVI phenomenon is shifted towards larger advance ratios.

Blade–vortex and vortex–vortex interactions between main rotor and tail rotor. The tip vortices of the Bo105 main rotor (MR) interact with both the blades and the tip vortices of the tail rotor (TR) due the MR wake skew in forward flight. An example for this phenomenon is shown in Fig. 30. The two-bladed TR turns 5.2 times faster than the MR, and it is mounted on the port side of the helicopter. It acts as a pusher; hence, the TR tip vortices convect away from both the tailboom and the cameras. The rotation directions of MR and TR are indicated by black arrows. The interaction takes place after the TR blade has cut through the MR tip vortex at an age of about $\Psi_V = 120°$, which causes the MR vortex to wrap around and, for a short time period, merge with the TR vortex.

A better understanding of the interaction process is provided by a schlieren time series, with the snapshot in Fig. 30 defining $t = 0$. At $t = -14.3$ ms (Fig. 31(a)), rotor blades from both MR and TR are visible, along with their newly shed tip vortices. Tip vortex II originates from the preceding MR blade passage. The lower branch is on the retreating side of the MR plane, and the upper branch is on the advancing side

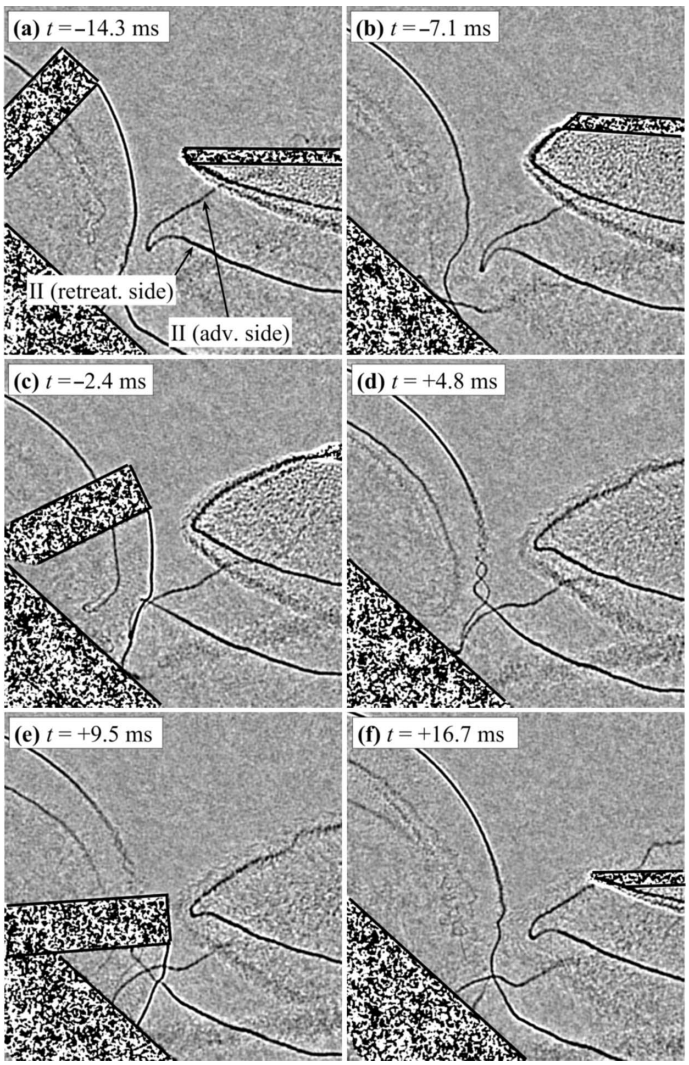

Fig. 31. Time series of the MR–TR interaction, $t = 0$ corresponds to Fig. 30.

due to the camera perspective. Vortex II successively approaches the TR flow and develops a bulge-like distortion of the vortex filament in its rearmost part (Fig. 31(b)). The tip of the following TR blade has just sliced through vortex II at $t = -2.4$ ms (Fig. 31(c)). The resulting interaction creates a double-helix, corkscrew-like structure seen between $t = 0$ (Fig. 30) and $t = 4.8$ ms (Fig. 31(d)). In particular, the retreating (lower) part of the MR tip vortex and the upper part of the TR tip vortex are wrapped around each other on a spiraling path. The vortex axes are roughly orthogonal in their initial condition, but joining both filaments yields corotation with the same rotational sense. However, a deeper understanding of the interaction mechanism based on the current data is difficult, due to the two-dimensional schlieren projection of a highly three-dimensional process, and since the BOS temporal resolution of 420 Hz is low in comparison to the fast-spinning TR. The double-helix interaction dissolves over the next few milliseconds and is barely visible above the next TR blade passage at $t = 9.5$ ms (Fig. 31(e)). The corresponding TR tip vortex again picks up the retreating branch of MR tip vortex II, and for a short time period around $t = 16.7$ ms in Fig. 31(f) a common MR-TR vortex filament is established. A quarter MR revolution is almost finished, and the next MR tip vortex starts to develop the bulge-like distortion towards the tail, repeating the entire process.

The MR–TR interaction phenomenon was consistently observed for Bo105 test points in the range of $0.2 < \mu^* \leq 0.7$. The BOS signal strength of the TR tip vortices and the vortex interaction decreased for higher flight speeds, which can be explained by an increasing directional stability of the tailboom and a decreasing thrust requirement of the TR. The EC135 rotorcraft does not produce similar interactions over the tailboom, as it uses a shrouded multibladed rotor–stator setup ("fenestron").

Conclusions

The rotor wakes of two free-flying helicopters IGE, the Airbus Bo105 and EC135, were investigated by means of BOS measurements and CTA. The study is a follow-up to a preceding experimental campaign with an improved setup and a wider range of test conditions, considering hover, vertical takeoff, and level flight cases. A particular focus was set on the wake dynamics and the influence of environmental conditions. The results can be summarized as follows:

1) The combination of large-field schlieren measurements and pointwise constant temperature sensors proved to be a good combination for a deeper insight into the flow structure around full-scale helicopters. The measurements benefit from recent developments in high-speed, high-resolution cameras and cost-effective fiber film sensors.

2) Tip vortex pairing was found to be a decisive and repeatable phenomenon in the wake of one of the helicopters (Bo105). The pairing occurred at an age corresponding to about one to two revolutions below the rotor plane, and it amplified local deflections of the involved vortex filaments. The paired structures mostly fell below the BOS detection limit soon after, but their footprint was detected further downstream in the wake by means of 2/rev-harmonic velocity signals with a strong radial coherence.

3) The other helicopter (EC135) did not produce a detectable vortex pairing within the measurement region. This led to a longer lifespan of the evenly spaced tip vortices, before dissolving due to noncooperative instabilities at higher vortex ages. Vortex pairing is known to be triggered by small initial perturbations, such as dissimilarities of the individual rotor blades, which can result from an imperfect blade tracking. It is not known whether the different aerodynamic design of the blades plays an additional role in the amplification of perturbations.

4) The rotor wake's shape and its average velocity profile strongly depend on the environmental wind conditions. For similar wind conditions, the current results agree well to preceding test campaigns.

5) Apart from a rather small influence of the tip-vortex–related harmonics, the velocity signals measured in the wake's radial slice plane closely followed Kolmogorov's power law, indicating broad-banded and well-developed turbulence.

6) The rotor wake structure for rapid vertical takeoff maneuvers with the Bo105 is similar to hover. When exceeding a hub height of approximately $h = 1.4$ rotor radii or 6.8 m, the wake structure changed to large-scale low-frequency velocity oscillations close to the ground.

7) The CTA sensors confirmed the categorization of forward-flight flow regimes depending on the normalized advance ratio, for example, the creation of a recirculation or ground vortex ahead of the helicopter.

8) Orthogonal BVI occurred in the frontal tip region of the rotor plane during forward flight and was visualized by schlieren images. The interaction depends on the advance ratio, which affects the local tip vortex trajectory and the resulting miss distance to the subsequent blade passage.

9) In forward flight, the Bo105's main rotor tip vortices convect along the skewed wake boundary and interact with the blades and tip vortices of the tail rotor. This phenomenon was not observed for the shrouded-rotor fenestron design of the EC135.

Acknowledgments

This study was conducted within the framework of the DLR projects "FAST Rescue" and "URBAN Rescue." The authors would like to thank Andreas Goerttler, Felix Wienke, Felix Lößle, Markus Krebs, and the "Flight Experiments" team of DLR Braunschweig for their help during the preparation and execution of the experiments.

References

[1]Schwarz, C., Bauknecht, A., Wolf, C. C., Coyle, A., and Raffel, M., "A Full-Scale Rotor-Wake Investigation of a Free-Flying Helicopter in Ground Effect Using BOS and PIV," *Journal of the American Helicopter Society*, **65**, 032007 (2020), DOI: 10.4050/JAHS.65.032007.

[2]Martin, P. B., Pugliese, G. J., and Leishman, J. G., "High Resolution Trailing Vortex Measurements in the Wake of a Hovering Rotor," *Journal of the American Helicopter Society*, Vol. 48, (1), January 2003, pp. 39–52, DOI: 10.4050/JAHS.48.39.

[3]Lee, T. E., Leishman, J. G., and Ramasamy, M., "Fluid Dynamics of Interacting Blade Tip Vortices with a Ground Plane," *Journal of the American Helicopter Society*, **55**, 022005 (2010), DOI: 10.4050/JAHS.55.022005.

[4]Ferguson, S. W., "Rotorwash Analysis Handbook: Volume I – Development and Analysis," DOT/FAA/RD-93/31, 1994.

[5]Ramasamy, M., and Yamauchi, G. K., "Using Model-Scale Tandem-Rotor Measurements in Ground Effect to Understand Full-Scale CH-47D Outwash," *Journal of the American Helicopter Society*, **62**, 012004 (2017), DOI: 10.4050/JAHS.62.012004.

[6]Light, J. S., "Tip Vortex Geometry of a Hovering Helicopter Rotor in Ground Effect," *Journal of the American Helicopter Society*, Vol. 38, (2), April 1993, pp. 34–42, DOI: 10.4050/JAHS.38.34.

[7]Rauleder, J., and Leishman, J. G., "Flow Environment and Organized Turbulence Structures Near a Plane Below a Rotor," *AIAA Journal*, Vol. 52, (1), January 2014, pp. 146–161, DOI: 10.2514/1.J052315.

[8]Tanner, P. E., Overmeyer, A. D., Jenkins, L. N., Yao, C.-S., and Bartram, S. M., "Experimental Investigation of Rotorcraft Outwash in Ground Effect," Proceedings of the 71th Annual Forum of the American Helicopter Society, Virginia Beach, VA, May 5–7, 2015.

[9]Milluzzo, J., and Leishman, J. G., "Fluid Dynamics of the Helicoidal Wake Sheets Trailed from a Hovering Rotor," *Journal of the American Helicopter Society*, **61**, 012002 (2016), DOI: 10.4050/JAHS.61.012002.

[10]Milluzzo, J. I., III, and Leishman, J. G., "Vortical Sheet Behavior in the Wake of a Rotor in Ground Effect," *AIAA Journal*, Vol. 55, (1), January 2017, pp. 24–35, DOI: 10.2514/1.J054498.

[11]Milluzzo, J. I., Martinez, A., Drayton, S., and Davis, S., "Experimental Investigation of Rotors Hovering Above Inclined Surfaces," *Journal of the American Helicopter Society*, **66**, 022005 (2021), DOI: 10.4050/JAHS.66.022005.

[12]Bourne, K., Reddy, K. R., Kumar, C., and Ooi, A., "An Investigation of Fundamental Flow Structures in Ground Effect with Application to the Development of Brownout Conditions in Hover," Proceedings of the 40th European Rotorcraft Forum, Southampton, UK, September 2–5, 2014.

[13]Ramasamy, M., and Leishman, J. G., "Interdependence of Diffusion and Straining of Helicopter Blade Tip Vortices," *Journal of Aircraft*, Vol. 41, (5), September 2004, pp. 1014–1024, DOI: 10.2514/1.3364.

[14]Kindler, K., Mulleners, K., Richard, H., van der Wall, B., and Raffel, M., "Aperiodicity in the Near Field of Full-Scale Rotor Blade Tip Vortices," *Experiments in Fluids*, Vol. 50, (6), June 2011, pp. 1601–1610, DOI: 10.1007/s00348-010-1016-8.

[15]Kutz, B. M., Keßler, M., and Krämer, E., "Experimental and Numerical Examination of a Helicopter Hovering in Ground Effect," *CEAS Aeronautical Journal*, Vol. 4, (4), December 2013, pp. 397–408, DOI: 10.1007/s13272-013-0084-x.

[16]Sugiura, M., Tanabe, Y., Sugawara, H., Matayoshi, N., and Ishii, H., "Numerical Simulations and Measurements of the Helicopter Wake in Ground Effect," *Journal of Aircraft*, Vol. 54, (1), January 2017, pp. 209–219, DOI: 10.2514/1.C033665.

[17]Silva, M. J., and Riser, R., "CH-47D Tandem Rotor Outwash Survey," Proceedings of the 67th Annual Forum of the American Helicopter Society, Virginia Beach, VA, May 3–5, 2011.

[18]Wadcock, A. J., Ewing, L. A., Solis, E., Potsdam, M., and Rajagopalan, G., "Rotorcraft Downwash Flow Field Study to Understand the Aerodynamics of Helicopter Brownout," Proceedings of the American Helicopter Society Southwest Region Technical Specialists' Meeting, Dallas, TX, October 15–17, 2008.

[19]Wong, O. D., and Tanner, P. E., "Photogrammetric Measurements of an EH-60L Brownout Cloud," *Journal of the American Helicopter Society*, **61**, 012003 (2016), DOI: 10.4050/JAHS.61.012003.

[20]Michaelsen, O., "A Comparison of Outflows from a Helicopter, Tilt Wing and Jet Lift Hovering Aircraft," AIAA 1971-992, Proceedings of the 8th AIAA Annual Meeting and Technical Display, Washington, DC, October 25–28, 1971, DOI: 10.2514/6.1971-992.

[21]Milluzzo, J., Sydney, A., Rauleder, J., and Leishman, J. G., "In-Ground-Effect Aerodynamics of Rotors with Different Blade Tips," Proceedings of the 66th Annual Forum of the American Helicopter Society, Phoenix, AZ, May 11–13, 2010.

[22]Schwarz, C., Bauknecht, A., Mailänder, S., and Raffel, M., "Wake Characterization of a Free-Flying Model Helicopter in Ground Effect," *Journal of the American Helicopter Society*, **64**, 012010 (2019), DOI: 10.4050/JAHS.64.012010.

[23]Ramasamy, M., Potsdam, M., and Yamauchi, G. K., "Measurements to Understand the Flow Mechanisms Contributing to Tandem-Rotor Outwash," Proceedings of the 71st Annual Forum of the American Helicopter Society, Virginia Beach, VA, May 21–23, 2015.

[24]Sheridan, P. F., and Wiesner, W., "Aerodynamics of Helicopter Flight Near the Ground," Proceedings of the 33rd Annual Forum of the American Helicopter Society, Washington, DC, May 9–11, 1977.

[25]Curtiss, H. C., Sun, M., Putman, W. F., and Hanker, E. J., "Rotor Aerodynamics in Ground Effect at Low Advance Ratios," *Journal of the American Helicopter Society*, Vol. 29, (1), January 1984, pp. 48–55, DOI: 10.4050/JAHS.29.48.

[26]Ganesh, B., and Komerath, N., "Study of Ground Vortex Structure of Rotorcraft in Ground Effect at Low Advance Ratios," AIAA 2006-3475, Proceedings of the 24th AIAA Applied Aerodynamics Conference, San Francisco, CA, June 5–8, 2006, DOI: 10.2514/6.2006-3475.

[27]Nathan, N. D., and Green, R. B., "Measurements of a Rotor Flow in Ground Effect and Visualisation of the Brown-Out Phenomenon," Proceedings of the 64th Annual Forum of the American Helicopter Society, Montréal, Canada, April 29-May 1, 2008.

[28]Nathan, N. D., and Green, R. B., "The Flow Around a Model Helicopter Main Rotor in Ground Effect," *Experiments in Fluids*, Vol. 52, (1), January 2012, pp. 151–166, DOI: 10.1007/s00348-011-1212-1.

[29]Saijo, T., Ganesh, B., Huang, A., and Komerath, N. M., "Development of Unsteadiness in a Rotor Wake in Ground Effect," AIAA 2003-3519, Proceedings of the 21st AIAA Applied Aerodynamics Conference, Orlando, FL, June 23–26, 2003, DOI: 10.2514/6.2003-3519.

[30]Ganesh, B., and Komerath, N., "Unsteady Aerodynamics of Rotorcraft in Ground Effect," AIAA 2004-5287, Proceedings of the 22nd AIAA Applied Aerodynamics Conference and Exhibit, Providence, RI, August 16–19, 2004, DOI: 10.2514/6.2004-5287.

[31]Ganesh, B., Komerath, N., Pulla, D., and Conlisk, A. T., "Unsteady Aerodynamics of Rotorcraft in Ground Effect," AIAA 2005-1407, Proceedings of the 43rd AIAA Aerospace Sciences Meeting and Exhibit, Reno, NV, January 10–13, 2005, DOI: 10.2514/6.2005-1407.

[32]Bauknecht, A., Ewers, B., Wolf, C., Leopold, F., Yin, J., and Raffel, M., "Three-Dimensional Reconstruction of Helicopter Blade-Tip Vortices Using a Multi-Camera BOS System," *Experiments in Fluids*, Vol. 56, 1866 (2015), DOI: 10.1007/s00348-014-1866-6.

[33]Ramasamy, M., and Leishman, J. G., "A Generalized Model for Transitional Blade Tip Vortices," *Journal of the American Helicopter Society*, Vol. 51, (1), January 2006, pp. 92–103, DOI: 10.4050/1.3092881.

[34]Holzäpfel, F., Hofbauer, T., Darracq, D., Moet, H., Garnier, F., and Ferreira Gago, C., "Analysis of Wake Vortex Decay Mechanisms in the Atmosphere," *Aerospace Science and Technology*, Vol. 7, (4), June 2003, pp. 263–275, DOI: 10.1016/S1270-9638(03)00026-9.

[35]Leishman, J. G., *Principles of Helicopter Aerodynamics*, second edition, Cambridge University Press, New York, NY, 2006, Chapters 3.3.8 and 3.5.2.

[36]Bauknecht, A., Schwarz, C., Raffel, M., and Mailänder, S., "Flow Measurement Techniques for Rotor Wake Characterization on Free-Flying Helicopters in Ground Effect," AIAA 2019-2107, Proceedings of the AIAA Scitech 2019 Forum, San Diego, CA, January 7–11, 2019, DOI: 10.2514/6.2019-2107.

[37]Richter, K., Koch, S., Goerttler, A., Lütke, B., Wolf, C. C., and Benkel, A., "Unsteady Boundary Layer Transition on the DSA-9A Rotor Blade Airfoil," Proceedings of the 41st European Rotorcraft Forum, Munich, Germany, September 1–4, 2015.

[38]Bruun, H. H., *Hot-Wire Anemometry: Principles and Signal Analysis*, Oxford University Press, Oxford, UK, 1995, pp. 28–32.

[39]Freymuth, P., "Calculation of Square Wave Test for Frequency Optimised Hot-Film Anemometers," *Journal of Physics E: Scientific Instruments*, Vol. 14, (2), 1981, pp. 238–240, DOI: 10.1088/0022-3735/14/2/021.

[40]Norman, T. R., and Light, J. S., "Rotor Tip Vortex Geometry Measurements Using the Wide-Field Shadowgraph Technique," *Journal of the American Helicopter Society*, Vol. 32, (2), April 1987, pp. 40–50, DOI: 10.4050/JAHS.32.40.

[41]Heineck, J. T., Banks, D. W., Smith, N. T., Schairer, E. T., Bean, P. S., and Robillos, T., "Background-Oriented Schlieren Imaging of Supersonic Aircraft in Flight," *AIAA Journal*, Vol. 59, (1), January 2021, pp. 11–21, DOI: 10.2514/1.J059495.

[42]Leopold, F., "The Application of the Colored Background Oriented Schlieren Technique (CBOS) to Free-Flight and In-Flight Measurements," Proceedings of the 22nd International Congress on Instrumentation in Aerospace Simulation Facilities, Pacific Grove, CA, June 10–14, 2007, DOI: 10.1109/ICIASF.2007.4380894.

[43]Raffel, M., Heineck, J. T., Schairer, E., Leopold, F., and Kindler, K., "Background-Oriented Schlieren Imaging for Full-Scale and In-Flight Testing," *Journal of the American Helicopter Society*, **59**, 012002 (2014), DOI: 10.4050/JAHS.59.012002.

[44]Bauknecht, A., Merz, C. B., Raffel, M., Landolt, A., and Meier, A. H., "Blade-Tip Vortex Detection in Maneuvering Flight Using the Background-Oriented Schlieren Technique," *Journal of Aircraft*, Vol. 51, (6), November 2014, pp. 2005–2014, DOI: 10.2514/1.C032672.

[45]van der Wall, B., *Grundlagen der Hubschrauber-Aerodynamik*, Springer Verlag, Berlin, Germany, 2015, pp. 364–367.

[46]Kampa, K., Enenkl, B., Polz, G., and Roth, G., "Aeromechanic Aspects in the Design of the EC135," *Journal of the American Helicopter Society*, Vol. 44, (2), April 1999, pp. 83–93, DOI: 10.4050/JAHS.44.83.

[47]Welch, P. D., "The Use of Fast Fourier Transform for the Estimation of Power Spectra: A Method Based on Time Averaging over Short, Modified Periodograms," *IEEE Transactions on Audio Electroacoustics*, Vol. 15, (2), June 1967, pp. 70–73, DOI: 10.1109/TAU.1967.1161901.

[48]Wolf, C. C., Braukmann, J. N., Stauber, W., Schwermer, T., and Raffel, M., "The Tip Vortex System of a Four-Bladed Rotor in Dynamic Stall Conditions," *Journal of the American Helicopter Society*, **64**, 022005 (2019), DOI: 10.4050/JAHS.64.022005.

[49]Caradonna, F., "Performance Measurement and Wake Characteristics of a Model Rotor in Axial Flight," *Journal of the American Helicopter Society*, Vol. 44, (2), April 1999, pp. 101–108, DOI: 10.4050/JAHS.44.101.

[50]Ohanian, C. V., McCauley, G. J., and Savaş, Ö., "Performance Measurement and Wake Characteristics of a Model Rotor in Axial Flight," *Journal of the American Helicopter Society*, **57**, 042005 (2012), DOI: 10.4050/JAHS.57.042005.

[51]Sherry, M., Nemes, A., Lo Jacono, D., Blackburn, H. M., and Sheridan, J., "The Interaction of Helical Tip and Root Vortices in a Wind Turbine Wake," *Physics of Fluids*, **25**, 117102 (2013), DOI: 10.1063/1.4824734.

[52]Bolnot, H., Le Dizès, S., and Leweke, T., "Pairing Instability in Helical Vortices," *Wind Energy—Impact of Turbulence*, edited by M. Hölling, Vol. 2, Chap. 6, Springer Verlag, Berlin, Germany, 2014, pp. 23–28, DOI: 10.1007/978-3-642-54696-9_4.

[53]Taylor, G. I., "The Spectrum of Turbulence," *Proceedings of the Royal Society London A*, Vol. 164, (919), February 1938, pp. 476–490, DOI: 10.1098/rspa.1938.0032.

[54]Tangler, J. L., "Schlieren and Noise Studies of Rotors in Forward Flight," Proceedings of the 33rd Annual Forum of the American Helicopter Society, Washington, DC, May 9–11, 1977.

[55]Chen, R. T. N., "A Survey of Nonuniform Inflow Models for Rotorcraft Flight Dynamics and Control Applications," NASA TM 102219, 1989.

[56]Komerath, N., Wong, O., and Ganesh, B., "On the Formation and Decay of Rotor Blade Tip Vortices," AIAA 2004-2431, Proceedings of the 34th AIAA Fluid Dynamics Conference and Exhibit, Portland, OR, June 28–July 1, 2004, DOI: 10.2514/6.2004-2431.